

UNIVERSITY of CALIFORNIA
SANTA CRUZ

**TIDAL DISRUPTIONS OF MAIN SEQUENCE STARS OF VARYING
MASS AND AGE: INFERENCES FROM THE COMPOSITION OF
THE FALLBACK MATERIAL**

A thesis submitted in partial satisfaction of the
requirements for the degree of

BACHELOR OF SCIENCE

in

PHYSICS

by

Monica P. Gallegos-Garcia

10 June 2018

The thesis of Monica P. Gallegos-Garcia is approved by:

Professor Enrico Ramírez-Ruiz
Advisor

Professor Alexander Sher
Senior Theses Coordinator

Professor Robert Johnson
Chair, Department of Physics

Copyright © by

Monica P. Gallegos-Garcia

2018

Abstract

Tidal Disruptions of Main Sequence Stars of Varying Mass and Age: Inferences from the Composition of the Fallback Material

by

Monica P. Gallegos-Garcia

We use a simple framework to calculate the time evolution of the composition of the fallback material onto a supermassive black hole arising from the tidal disruption of main sequence stars. We study stars with masses between 0.8 and 3.0 M_{\odot} , at evolutionary stages from zero-age main sequence to terminal-age main sequence, built using the Modules for Experiments in Stellar Astrophysics code. We show that most stars develop enhancements in nitrogen (^{14}N) and depletions in carbon (^{12}C) and oxygen (^{16}O) over their lifetimes, and that these features are more pronounced for higher mass stars. We find that, in an accretion-powered tidal disruption flare, these features become prominent only after the time of peak of the fallback rate and appear at earlier times for stars of increasing mass. We postulate that no severe compositional changes resulting from the fallback material should be expected near peak for a wide range of stellar masses and, as such, are unable to explain the extreme helium-to-hydrogen line ratios observed in some TDEs. On the other hand, the resulting compositional changes could help explain the presence of nitrogen-rich features, which are currently only detected after peak. When combined with the shape of the light curve, the time evolution of the composition of the fallback material provides a clear method to help constrain the nature of the disrupted star. This will enable a better characterization of the event by helping break the degeneracy between the mass of the star and the mass of the black hole when fitting tidal disruption light curves.

Contents

List of Figures	v
Dedication	viii
Acknowledgements	ix
1 Introduction	1
2 Background	4
2.1 Stellar Evolution	4
2.2 The Mass Accretion Rate	7
3 Methods	10
3.1 Stellar Models	13
3.2 Salient Model Features	14
4 The Disruption of Evolved MS Stars	17
4.1 Tidal Vulnerability	17
4.2 The Disruption of a Sun-like Star	18
4.3 Disruption of MS stars	22
5 Discussion	28
5.1 Summary of Key Results	28
5.2 Implications for Observations and Models	29
Bibliography	33
6 Appendix	36
6.1 Publication	36

List of Figures

2.1	Simple illustration of a tidal disruption event. In this scenario the star approaches a SMBH on a parabolic trajectory. At r_t the star is disrupted and half of its stellar debris becomes bound to the SMBH and will be accreted during its next pericenter passage. This image was reconstructed from [1].	7
2.2	Artist rendition of an accretion disc around a black hole [2].	9
3.1	The geometry of the disrupted star and how it can be used to calculate dM/dE . The orange slice represents an equal orbital binding energy surface, which can be approximated as an equal fallback time surface. Here x is the distance from the center of the star along the star's orbital plane and H_x is the maximum radius of the particular slice. When calculating the equal arrival time surfaces it is common to neglect any azimuthal or polar deviations. These can be safely neglected given that $(R_*/r_t) = q^{1/3} \ll 1$	11
3.2	The rate of fallback of stellar debris to pericenter as a function of time from the disruption of a $1M_\odot$ star calculated using the analytic framework used in this work (<i>thick dark blue</i> line), which assumes a full disruption, compared to those calculated by [3] using hydrodynamical calculations for different β values (<i>thin colored</i> lines). Both calculations use $M_{\text{bh}} = 10^6 M_\odot$ and a star that is constructed as a self-gravitating, spherically symmetric, polytropic fluid with $\gamma = 5/3$	12
3.3	Compositional abundance as a function of enclosed mass in a $1M_\odot$ star at three different evolutionary stages during its MS lifetime. In this paper, we characterize evolutionary stages by f_{H} , the fraction of central hydrogen that has been burned. Here we show the stellar profiles for $f_{\text{H}} = 0.0 = f_{\text{ZAMS}}$ (<i>dotted</i>), $f_{\text{H}} = 0.60$ (<i>dashed</i>), and $f_{\text{H}} = 0.99$ (<i>solid</i>), respectively. A $1M_\odot$ star disrupted at later stages in its evolution should reveal abundance anomalies: an increase in nitrogen and depletion of oxygen, as previously argued by [4].	15
3.4	Density profiles for a $1M_\odot$ star at different times along its MS evolution. The <i>red</i> line corresponds to ZAMS with a central density of 81 g cm^{-3} and the <i>pink</i> line corresponds to a central hydrogen fraction of 10^{-3} with a central density of 500 g cm^{-3} . These different density profiles result in different r_t and thus exhibit different vulnerability to disruption.	16

- 4.1 In both panels, the color scale shows the tidal radius of the disrupted star. *Left panel:* Plotted are the ratio of the star’s tidal radius to the tidal radius of that same star at ZAMS ($f_H = 0.0 = f_{ZAMS}$). This shows that the star’s vulnerability to disruption increases with age. This effect is stronger for more massive stars. *Right panel:* Plotted are the ratio of the tidal radius to $r_{t,burn}$. Here $r_{t,burn}$ is defined as the tidal radius of the star’s core undergoing active nuclear burning, where the specific power from nuclear reactions is greater than $1 \text{ erg g}^{-1}\text{s}^{-1}$. This shows that all of the stars in our study require deeper encounters to strip mass from their burning regions. 18
- 4.2 Mass fallback rates for elements that make up 99.6% of the mass of a $1M_\odot$ tidally disrupted star at two different evolutionary stages. The star aged nearly 5 Gyr from the *dotted* lines ($f_H = 0.0 = f_{ZAMS}$) to the *solid* lines ($f_H = 0.60$). \dot{M} for the total mass of the star is shown by the *gray* curves. All curves are normalized to \dot{M}_{peak} and t_{peak} for the corresponding ZAMS star. The main changes in fallback rates as the star evolves along the MS are an increase in nitrogen and a decrease in carbon after t_{peak} due to CNO activity in the core. 19
- 4.3 The fallback rate for different elements, \dot{M}_X , following the disruption of a $1M_\odot$ star at three different evolutionary stages. The *left* and *center* panels correspond to the *dotted* and *solid* lines shown in Figure 4.2, respectively. The *right* panel shows \dot{M} for the same star but at $f_H = 0.99$, which corresponds to an age of 8.3 Gyr. Time is in units of t_{peak} . As the star ages we see an increase in nitrogen and a decrease in carbon abundance but only after t_{peak} 20
- 4.4 Elemental abundance of the fallback material relative to solar following the disruption of a $1M_\odot$ at two different evolutionary stages: $f_H = 0.60$ (*left* panel) and TAMS (*right* panel). A rapid evolution of ^{14}N and ^{12}C abundance relative to the other elements is clearly seen. The solar ratios clearly illustrate the significance of the variations in the abundances of ^{16}O , ^4He , and ^{20}Ne 21
- 4.5 The relative abundance of stellar debris as a function of fallback time arising from the disruption of $0.8M_\odot$ (*top* row), $2.0M_\odot$ (*middle* row) and $3.0M_\odot$ (*bottom* row) stars at three different evolutionary stages ($f_H = 0.3, 0.6$ and 0.99). The change in abundance relative to solar is observed to increase with mass and age but only after t_{peak} . These anomalies appear at earlier times for higher mass stars. 22
- 4.6 Elemental abundances relative to solar at the time the mass fallback rate has reached one tenth of its peak value, $t_{0.1} > t_{peak}$, for all of the stellar masses and ages in our sample. Elements of interest are ^{12}C , ^4He , ^{14}N and ^{16}O . Values are shown as a function of the star’s fractional main sequence lifetime and stellar mass. We find carbon abundances to be more indicative of stellar mass for $M_\star \lesssim 1.5M_\odot$, while helium abundances are correlated with stellar age for all masses. $(X/X_\odot)_{^{14}\text{N}} \gtrsim 5.0$ occurs only for masses greater than $1.5M_\odot$ and develops early in the star’s evolution. We also find oxygen abundances to be primarily stellar mass dependent. 24
- 4.7 Same as Figure 4.6 but presented with stellar age in years (x -axis). The white regions correspond to pre-MS (*left*) or post-MS (*right*). 25
- 4.8 Fallback abundance at $t_{0.1}$ of ^4He , ^{12}C , ^{14}N , and ^{16}O (clockwise from top left) for the disruption (by a $M_{bh} = 10^6 M_\odot$ SMBH) of $0.8M_\odot$, $1M_\odot$, $1.2M_\odot$, $1.4M_\odot$, $2.0M_\odot$, and $3.0M_\odot$ stars along their MS evolution. Abundances are at $t_{0.1}$, but points are placed at \dot{M}_{peak} and t_{peak} for the disruption of each star. Abundances are quoted relative to solar. Points are roughly equally spaced in time for each mass, with the top-left-most point being ZAMS and the bottom-right-most point being TAMS. (This is not strictly true for the ZAMS point of the $1M_\odot$, $1.2M_\odot$, and $1.4M_\odot$ stars as their radius slightly decreases at the very beginning of their MESA evolution, but all other points for these stars proceed left to right with age as the star subsequently evolves.) 27

- 5.1 The ratio of t_{burn} to t_{peak} as a function of f_{H} and stellar mass. Here t_{burn} is the time when non-solar abundance ratios begin to appear in the fallback material, specifically when the abundance of ^{12}C and ^{14}N deviate from solar. We have explicitly excluded $f_{\text{H}} \lesssim 0.05$ from this plot, given that these stars experience some mild contraction early in their MESA evolution. The ratio ($t_{\text{burn}}/t_{\text{peak}}$) reaches a maximum (minimum) value of 7.6 (1.15) for a $0.8M_{\odot}$ ($3M_{\odot}$) star at $f_{\text{H}} = 0.05$ ($f_{\text{H}} = 0.23$). 30
- 5.2 Compositional features in the spectra of well-sampled tidal disruption events with existing spectroscopic observations. The y - and x -axes show luminosity and time relative to peak respectively, with different colors corresponding to distinct events, and different symbols corresponding to different spectral features. We show the minimum values of $t_{\text{burn}}/t_{\text{peak}}$ (Figure 5.1) as derived from our study for a $1M_{\odot}$ (*dashed* line) and $3M_{\odot}$ (*dash-dotted* line) star. 31

Para, Mi mamá,

Margarita Garcia.

Acknowledgements

I would like to thank my research advisor, Enrico Ramírez-Ruiz, for his immense support and care. The opportunity to do research with such a talented and influential scientist and a genuinely kind person is a privilege I will never take for granted. Thank you for treating your students as friends. Thank you for always empowering me to believe in myself and giving me the space and opportunities to see that I am more than what society tells me.

I would like to thank STEM Diversity Programs and Yulianna Ortega for creating a community of scholars and allies within UCSC. Their invaluable services and programs have provided me with the mentorship, resources, and support that have allowed me to begin to thrive in academia.

Finally, I am eternally thankful for my friendships, participation, and experience in the Banneker and Aztlán Institute at Harvard University. My academic and personal accomplishments mean as much to me as they do to the mission of the program, to prepare talented undergraduate students of color and other underrepresented groups for studies in astronomy. Through the dedicated work of the Banneker and Aztlán mentors I have learned to see the scientist within me and the scientist I can be.

1 Introduction

We study supermassive black holes (SMBH) within galactic nuclei by analyzing the movement of stars swarming around them. When the conditions are right we can observe the black hole's destructive power. A tidal disruption event (TDE) begins when a star wanders too close to a SMBH. Through the combined influence of the SMBH's gravitational force and interactions with other stars, a star can be directed onto a nearly radial orbit towards the SMBH. This puts the star on a course to be squeezed and spun enough to break it apart. For a full disruption, approximately half of the stellar material is ejected out of the system on hyperbolic orbits while the other half becomes gravitationally bound to the black hole after the disruption and eventually accretes onto the black hole. This accretion creates a powerful flare that decays over a period of months [5].

These high-energy events can reveal once quiescent SMBHs at the centers of galaxies and are filled with physics yet to be fully modeled and understood. Observations in tandem with theoretical models are used to probe the physics that governs the disruption of the star and the dissipative processes that are responsible for radiating the acquired gravitational energy. For example, characteristic signatures in the models of TDEs have been used to study their general relativistic correction [6]. The study of the disruption of evolved stars has introduced characteristic timescales as theoretical models of these flares are shown to rise slowly and decay over many years, in contrast to the disruption of middle-aged sun-like stars. These evolved stars can also reveal the most massive SMBH ($\gtrsim 10^8 M_\odot$), a mass where other stars are swallowed whole without producing a luminous flare [7]. Additionally, thanks to observational progress, a recent study has proposed that the abundance pat-

terns present during a star’s evolution can lead to anomalous TDE emission features in observations [4].

In recent years we have seen an increase in the number of observed TDEs [8] and an increase in the quality of TDE observations taken with transient surveys such as the Palomar Transient Factory (PTF), the All-Sky Automated Survey for Supernovae (ASAS-SN) and the Panoramic Survey Telescope and Rapid Response System (Pan-STARRS) [9], [10], [11]. These observations have captured the evolution of some events at early times, a region not well observed in the past, and the evolution of the flares for months after its initial discovery [12, 13, 14]. These recent observations present a broader picture of the evolution of a TDE and have revealed a variety of new features.

Of importance to this thesis is the evolution of emission and absorption features seen in the spectrum of these sources. Specifically, we are interested in the wide range of helium to hydrogen ratios observed as well as events with strong nitrogen composition [11, 9, 15, 16]. The origin of these features is significantly debated. The extreme and non-solar hydrogen to helium ratios were initially proposed to be the disruption of a star with a helium-rich core [11]. However, it has been shown that for a specific configuration of stellar material, these non-solar abundance features can be produced from the radiative processes in TDEs—even when the stellar material is of solar composition [17]. As for the nitrogen features, these events have been proposed to be the disruption of evolved stars with significant nitrogen-producing nuclear activity [4]. It is important to understand the origin of these features and use the presence or absence of particular emission line features accurately as they can be used to probe the nature of the star before disruption [4, 18]. A clear description of these features requires a clear understanding of the radiative process that produce them and a study of composition of the stellar material involved. However, to date there has not been a complete analysis on how the composition of the stellar material evolves with time during a TDE ¹.

Motivated by this, we move beyond the standard analysis of the accretion rate to study the time evolution of the element composition in tidal disruption events for stars of various mass

¹Except for the specific case of a hydrogen-helium white dwarf [19].

and age. Through this analysis we address the on-going questions related to the origin of anomalous emission features in observed TDEs and expand upon previous work to further characterize the composition of the disrupted stellar debris. Our analysis includes the use of an analytical framework to model a TDE and analytically track the composition of the stellar material that will be accreted onto the SMBH and create a luminous flare. We make use of Modules for Experiments in Stellar Astrophysics (MESA) [20] to generate stars with realistic compositions and structures. This allows us to efficiently study a wide range of stars at different ages without the computational expense of hydrodynamical simulations. Our results predict at what time in the TDE an observer should expect to see large elemental deviation resulting from the stellar material. Additionally, our results predict what happens when stars of different masses and evolutionary states are tidally disrupted, and what composition a distant observer might be able to infer as the signature of such events. With this we can begin to use spectra features in TDEs to constrain the stellar mass and age for some well-studied events.

This thesis is structured as follows. In Chapter 2 I present background information necessary to understand the process of a tidal disruption event and briefly discuss stellar evolution features relevant to our study. In Chapter 3 I present our analytic procedure to tidally disrupt stars built using MESA, in Chapter 4 I present our results and discuss their implications in Chapter 5. Finally in Chapter 6 I present the published version of this work that was published in the *Astrophysics Journal*. A majority of the text in this thesis is taken from the publication.

Except where explicit reference is made to the work of others, the contents are original and are entirely the result of my own research. Parts of this work, which are specifically indicated in the text, have appeared in published form.

2 Background

2.1 Stellar Evolution

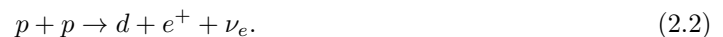
A star's life is determined by its mass. This controls its ability to balance the force due to its own self gravity and the outward force due to thermal gas pressure or radiation pressure. In this section I briefly describe how a star's features, such as radius and composition, evolve throughout its lifetime. The features discussed here are relevant to stars between $1 - 3M_{\odot}$ and are a result of different stellar masses and a star's individual evolution.

As a nebulous cloud of gas contracts to become a star, its thermal pressure increase and at a sufficient central temperature, nuclear fusion is ignited at the center of the star. This defines the beginning of the main sequence (MS). The temperature where this fusion ignites is empirical estimated as,

$$T_c \approx 1.5 \times 10^7 \left(\frac{M_{\star}}{M_{\odot}} \right)^{1/3}, \quad (2.1)$$

where M_{\star} is the mass of the star and M_{\odot} is one solar mass.

There are two main fusion processes in MS stars: the proton-proton (p-p) chain and the CNO cycle. These are highly sensitive to the central temperature of the star [21] and, given Equation 2.1, contribute differently to stars of varying mass. The p-p chain increases the abundance of ${}^4\text{He}$ in stars by fusing two protons via a weak nuclear reaction



The deuteron created in Equation 2.2 is then used for a second reaction,



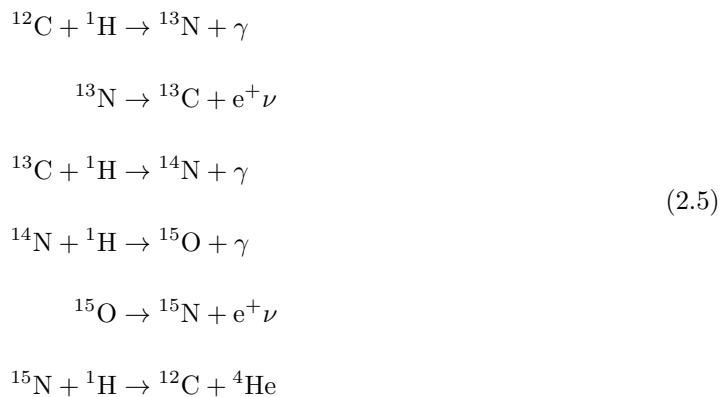
Following this, there exists three branches of reactions that all result in,



where Q_{eff} is the effective energy released by the branch. The three branches release 26.2MeV, 25.2MeV, and 19.1MeV and make up 85%, 15%, and 0.002% of the total reactions respectively [22].

The p-p chain roughly dominates the energy generation for masses $\lesssim 1.5 M_{\odot}$.

For stars with mass $\gtrsim 1.5 M_{\odot}$ the CNO cycle dominates. Equation 2.5 illustrates the main cycle.



During the reactions of Equation 2.5, fusing hydrogen to helium results in an increase of ${}^{14}\text{N}$ with ${}^{12}\text{C}$ acting as a catalyst for the entire cycle. A second cycle which branches from ${}^1\text{H}$ in the last reaction decreases ${}^{16}\text{O}$ abundance. With this, the evolution of specific elemental abundances can be used to infer the fusion processes responsible, and thus infer a mass range for that star.

Another stellar feature important in our study is a star's density. As a star evolves along the MS, its average density, $\bar{\rho}_{\star}$, decreases while its core density, ρ_{core} , increases. These changes are a result of the following. As hydrogen is fused into helium in the core of the star through the p-p chain or CNO cycle, the mean mass per particle, μ , increases. By the ideal gas law,

$$P_{\text{gas}} = \frac{\mathcal{R}}{\mu} \rho T, \quad (2.6)$$

the gas pressure P_{gas} decreases in this region. This lower pressure can no longer support the star against its own gravity as effectively as before and the core of the star contracts. This denser material will have a higher temperature and, combined with the increase of ρ_{core} , will cause P_{gas} to increase. As a result of the local increase in temperature at the core, the temperature gradient dT/dr across the star increases. This in turn increases radiative diffusion, the thermal conduction of heat by photons.

$$F = \frac{4ac}{3\rho\kappa} T^3 \frac{dT}{dr} \quad (2.7)$$

Equation 2.7 describes F the radiative flux density of heat by photons where κ is opacity, and a is a constant. This is a measurement of the flow of energy through the star. As this increase, the star's radius, R_{\star} , will increase.

The process summarized here occurs as μ increases throughout a star's MS lifetime and leads to a slow increase in R_{\star} . Since a star's mass remains constant during the MS, this process decrease the average density of a star $\bar{\rho}_{\star}$.

2.2 The Mass Accretion Rate

In this section I describe the process of a tidal disruption event by deriving the feeding rate \dot{M} of disrupted stellar material onto a SMBH. This rate gives rise to the luminosity we observe in these events and is a crucial element of our study in this thesis.

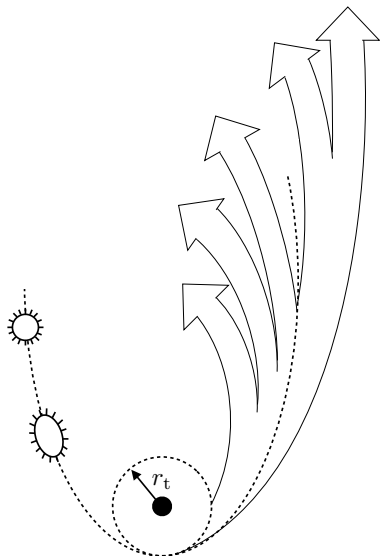


Figure 2.1: Simple illustration of a tidal disruption event. In this scenario the star approaches a SMBH on a parabolic trajectory. At r_t the star is disrupted and half of its stellar debris becomes bound to the SMBH and will be accreted during its next pericenter passage. This image was reconstructed from [1].

A tidal disruption event occurs when a star with mass M_* and radius R_* approaches a SMBH of mass M_{bh} on a parabolic orbit with pericenter distance, r_p , less than the tidal radius, r_t .

The tidal radius r_t is defined as the distance from the SMBH where the star's self-gravitational force is equal to the tidal force across the star due to the SMBH:

$$\frac{GM_*^2}{R_*^2} = \frac{GM_{\text{bh}}M}{r_t^3} R_* \quad (2.8)$$

$$r_t = \left(\frac{M_{\text{bh}}}{M_*} \right)^{1/3} R_*$$

A star within the tidal radius will be disrupted by the SMBH's tidal forces. The impact parameter $\beta \equiv r_t/r_p$ quantifies how deep the star penetrates into the tidal sphere (a sphere with radius r_t centered at the SMBH).

When a star is disrupted, the stellar debris will travel on approximately ballistic trajectories given by an orbital energy that is determined at r_t . An illustration of this is shown in Figure 2.1. These different orbital energies arise because during the disruption parts of the star are deeper in the potential of the SMBH than others. The total *spread* in specific energy of the stellar debris, E_t , can be approximated by taking the Taylor expansion of the SMBH's potential at the star's location:

$$E_t = \left. \frac{dU}{dr} \right|_{r_t} \Delta r \quad (2.9)$$

$$E_t = \frac{GM_{\text{bh}}}{r_t^2} R_* = q^{-1/3} E_*$$

where $E_\star = GM_\star/R_\star$ is the specific self-binding energy of the star, $q \equiv M_\star/M_{\text{bh}}$, and $\Delta r = R_\star$. This means that the change in orbital energy through the star is assumed to only be a result of stellar material's changing distance from the center (i.e. Δr in Equation 2.9). Since most tidally disrupted stars approach the SMBH on nearly parabolic orbits with zero orbital energy, E_t is also the energy of the most bound debris. This can be shown by taking the Taylor expansion of the star's orbital energy at r_t :

$$\begin{aligned} E &= (K + U)|_{r_t} + \frac{d}{dr} (K + U)|_{r_t} \Delta r \\ &= \frac{dU}{dr} \Big|_{r_t} \Delta r \\ &= \frac{GM_{\text{bh}}R_\star}{r_t^2} = q^{-1/3} E_\star = E_t. \end{aligned} \tag{2.10}$$

Here Δr is the distance from the center of the star and $K + U = 0$ since the center of mass orbital energy is nearly zero. Additionally, we also assumed that the kinetic energy K is constant throughout the star.

With E_t , we can also determine the fallback timescale for the most tightly bound debris, t_t . This is the time it takes for the disrupted stellar material with energy E_t to complete one orbit around the SMBH and return to r_t (see Figure 2.1). Using a Keplerian orbital period $t^2 = 4\pi^2 a^3 / (GM)$ and a relation between an orbit's semi-major axis and its orbital energy, $a = GM / (2E_t)$:

$$\begin{aligned} t_t &= \frac{\pi}{M_\star} \left(\frac{M_{\text{bh}} R_\star^3}{2G} \right)^{1/2} \\ &= 0.1 \text{ yr} \left(\frac{M_{\text{bh}}}{10^6 M_\odot} \right)^{1/2} \left(\frac{M_\star}{M_\odot} \right)^{-1} \left(\frac{R_\star}{R_\odot} \right)^{3/2}. \end{aligned} \tag{2.11}$$

Once the material returns to r_t , it forms an accretion flow around the SMBH. This is a hot disk of material that has lost a significant amount of energy by viscous dissipation and has circularized around the SMBH [23, 24, 25, 26]. An illustration of this is shown in Figure 2.2. These processes allow for the accretion, or the feeding, of stellar material into the SMBH. If the timescale for incoming material to lose energy by viscous dissipation is shorter than the fallback timescale t_t , the luminosity produced by the accretion will follow the rate that mass returns to the SMBH,

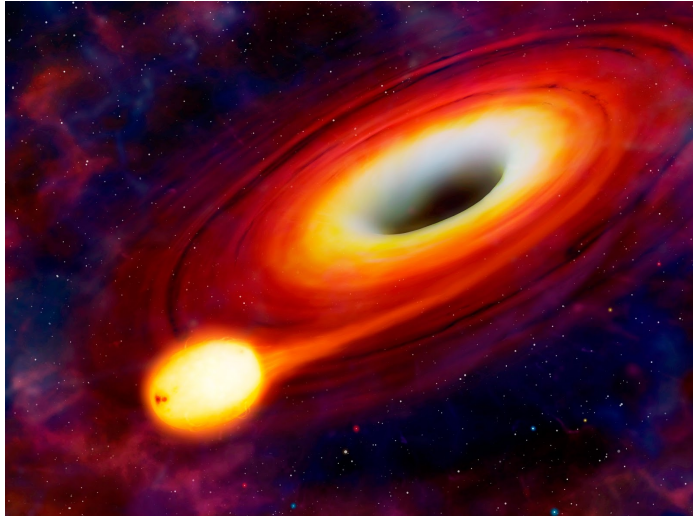


Figure 2.2: Artist rendition of an accretion disc around a black hole [2].

$$\dot{M} = \frac{dM}{dE} \frac{dE}{dt} = \frac{dM}{dE} \frac{1}{3} (2\pi G M_{\text{bh}})^{2/3} t^{-5/3} \quad (2.12)$$

Here dE/dt is found using the same methods as Equation 2.11 and dM/dE is the mass per specific orbital energy in the star. If this energy distribution dE/dM were constant throughout the entire star, $\dot{M} \propto t^{-5/3}$. However, this assumption has been shown to only valid at late times during the disruption [3, 27]. At early times, dM/dE depends on the distribution of mass in the disrupted star [27, 28] and the strength of the tidal interaction β [29, 30, 3].

More precise calculations of dM/dE require hydrodynamical simulations or careful analytical models to construct stars and explicitly calculate the energy distribution of the disrupted stellar debris. Such analytic models have been constructed to calculate dM/dE to $\mathcal{O}(q^{1/3})$ for stars described by a self-gravitating, spherically symmetric, star described with a polytropic equation of state [27, 31]. In this study we build on those analytic models to estimate the rate at which the debris falls back to pericenter is subsequently accreted. We extend their formalism to include information about the star's composition for tidally disrupted stars of varying mass and age with realistic density and composition profiles.

3 Methods

¹ The geometrical setup used in this study is shown in Figure 3.1. To calculate \dot{M} we begin by using the standard assumption that the star, and its orbital energy, *freezes in* at the moment of disruption at r_t . The specific binding energy of a fluid element in this case depends on its position. In our geometry, every element in a slice of our star, as in Figure 3.1, is safely assumed to be an equal distance from the SMBH and have equal orbital binding energy. In this case dM/dE can be expressed in terms of the star’s initial density profile ρ_* . The mass of a slice of stellar debris dM , defined here as having the same orbital energy, is found by integrating

$$\frac{dM}{dx} = \int_0^{H_x} \rho_*(h) 2\pi h dh, \quad (3.1)$$

where x is measured from the center of the star, H_x is the radius of the slice at a given x , and h is the rescaled height coordinate. If the orbital period t of a given slice is given in terms of its orbital binding energy dE/dx , then the rate dM/dt at which mass falls back to pericenter can be calculated by numerically integrating equation (3.1). Using this framework, we calculate the accretion rate history for a large number of realistic stars, whose density profiles we generate using the Modules for Experiments in Stellar Astrophysics (MESA) code. The reader is referred to Subsection 3.1 for a description of our MESA setup.

The use of this analytic method allows for an extensive study of \dot{M} arising from the disruption of different stars. While this formalism leads to a large reduction in computational expense, it is nonetheless restricted as it relies on the assumption of a spherically symmetric star at the time

¹Except for a few changes, this Chapter was taken from the publication.

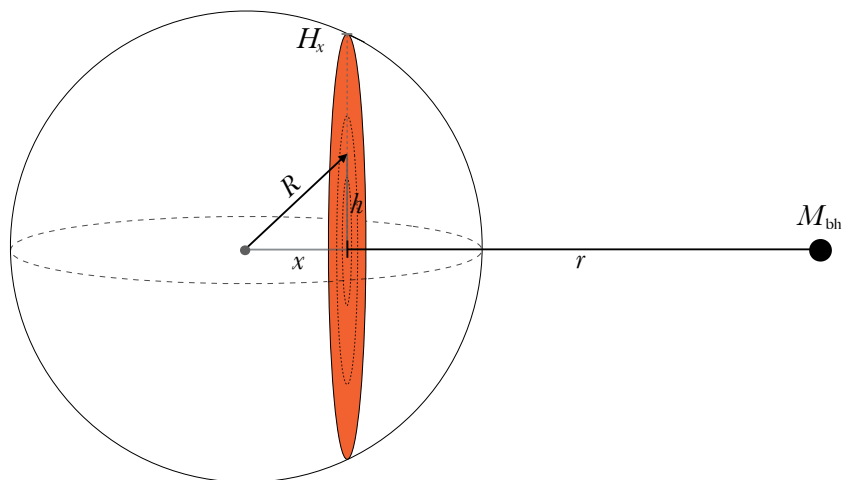


Figure 3.1: The geometry of the disrupted star and how it can be used to calculate dM/dE . The orange slice represents an equal orbital binding energy surface, which can be approximated as an equal fallback time surface. Here x is the distance from the center of the star along the star’s orbital plane and H_x is the maximum radius of the particular slice. When calculating the equal arrival time surfaces it is common to neglect any azimuthal or polar deviations. These can be safely neglected given that $(R_\star/r_t) = q^{1/3} \ll 1$.

of disruption. Contrary to what can be predicted by the simple analytical models used in this study, the rate at which material falls back depends strongly on the strength of the encounter, which can be measured by the penetration factor β .

This is because varying β changes the amount of mass lost by the star, which affects the rate at which the liberated stellar debris returns to pericenter (e.g.,[19]). In Figure 3.2 we compare fallback curves calculated using the analytical model (*thick dark blue* line) to those calculated using simulations (*thin colored* lines). For the purpose of comparison, both models use a $1M_\odot$ star with adiabatic index $\gamma = 5/3$ and a $10^6 M_\odot$ SMBH. We find that the broad features of \dot{M} are reasonably well captured by the simple model, as have been previously shown [27, 31]. This fact is extremely powerful in that it permits a reasonable characterization of TDE signatures without the need to run many computationally expensive simulations on the large set of stars we study here.

What is more, for a fixed β , the time evolution of the forces applied is identical, regardless of the ratio of the star’s mass to the mass of the SMBH. This is because the ratio of the time the star takes to cross pericenter, $t_p = r_p/v_{\text{esc}}$ to the star’s own dynamical time $t_{\text{dyn}} \equiv 1/\sqrt{\rho_\star G}$

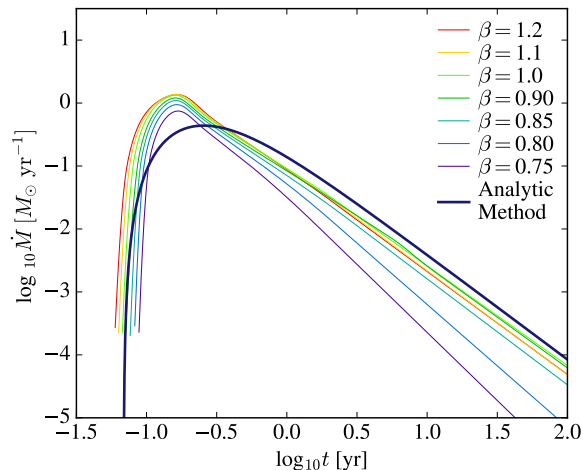


Figure 3.2: The rate of fallback of stellar debris to pericenter as a function of time from the disruption of a $1M_{\odot}$ star calculated using the analytic framework used in this work (*thick dark blue line*), which assumes a full disruption, compared to those calculated by [3] using hydrodynamical calculations for different β values (*thin colored lines*). Both calculations use $M_{\text{bh}} = 10^6 M_{\odot}$ and a star that is constructed as a self-gravitating, spherically symmetric, polytropic fluid with $\gamma = 5/3$.

depends only on β . Here v_{esc} is the characteristic velocity for this system and the dynamical time is analogous to how quickly information may travel through the star, Therefore, as long as $q \ll 1$, the tidal disruption problem is self-similar, and our results can be scaled to predict how the time (Equation 2.11) of peak accretion rate, t_{peak} , and its corresponding magnitude \dot{M}_{peak} change with M_{bh} , M_{\star} and R_{\star} :

$$\dot{M}_{\text{peak}} \propto M_{\text{bh}}^{-1/2} M_{\star}^2 R_{\star}^{-3/2}, \quad (3.2)$$

and

$$t_{\text{peak}} \propto M_{\text{bh}}^{1/2} M_{\star}^{-1} R_{\star}^{3/2}. \quad (3.3)$$

This fact is extremely powerful in that it permits us to completely characterize the properties of a disruption of a given star with one calculation. An exception to these simple scalings is if the star penetrates deeply enough such that r_{p} is comparable to the Schwarzschild radius, $r_{\text{g}} = GM_{\text{bh}}/c^2$. In this case, general relativistic effects can alter the outcome, especially if the black hole is spinning [29, 31].

We remind the reader that the exact value of the time of peak accretion rate t_{peak} and its

corresponding magnitude \dot{M}_{peak} are not precisely determined. Most of these differences arise from how the problem was originally formulated, in which the star’s self-gravity is ignored, and only the spread in binding energy across the star at pericenter is assumed to be important to determining \dot{M} . Our primary goal in this study is to develop a robust formalism for calculating the rate of fallback and its associated chemical composition as well as conducting a preliminary survey of the key stellar evolution parameters associated with this problem. The formalism presented in this section is well suited to this goal.

3.1 Stellar Models

We use the open source MESA code [20] to calculate the structure and composition of the stars that will be disrupted. We generated 192 solar metallicity stellar profiles ranging in mass from 0.8–3.0 M_{\odot} and evolutionary state from zero-age main sequence (ZAMS) to near the end of a star’s main sequence life time, terminal-age main sequence (TAMS). Profiles are spaced in intervals of 0.05 in central hydrogen fraction.

We consider the mass range of 0.8–3.0 M_{\odot} as stars with masses below 0.8 M_{\odot} will not evolve appreciably over the age of the universe, and stars with masses above 3 M_{\odot} , with MS lifetimes < 300 Myr, are unlikely to be disrupted since they evolve along the MS very quickly.

We do not consider evolved stars for two reasons. First, the contribution of evolved stars to the current and near-future tidal disruption population is expected to be modest [7]. Second, studies of the tidal disruption of evolved stars such as [7] have shown that even for large β , giant stars are effective at retaining envelope mass and effectively retaining their cores (where the differences in composition arise from MS and post-MS evolution). In this study we are interested in the evolved material in the inner-most layers of stars that can be reasonably revealed during a TDE and thus we do not focus on significantly evolved stars.

3.2 Salient Model Features

It has been argued previously that strong compositional variations are expected in the fallback material of MS stars [4]. In this study we trace the abundance variations of the following elements: ^1H , ^4He , ^{16}O , ^{12}C , ^{20}Ne , and ^{14}N . These elements make up at least 99.6% of each star’s total mass. The ^{34}S contribution and abundance ratio is very similar to that of ^{20}Ne and is thus not explicitly shown in this study. In what follows, we present abundances relative to solar.

As an example, in Figure 3.3 we show the compositional variations along the MS for a $1M_{\odot}$ star with solar abundance at ZAMS, the beginning of its main sequence lifetime. The differently styled lines correspond to different stellar ages as defined by f_{H} , the fraction of central hydrogen burned. A star will have $f_{\text{H}} = 0$ at ZAMS, and $f_{\text{H}} = 0.99$ near TAMS, the end of its MS lifetime. At ZAMS the star has solar composition (*dotted* lines) and is roughly homogeneous. After 4.8 Gyr (*dashed* lines), when more than half of the central hydrogen has been processed ($f_{\text{H}} = 0.60$), the following abundance variations are seen: a significant increase of ^{14}N , a modest increase (decrease) of ^4He (^1H), a significant decrease of ^{12}C , and a roughly unchanged abundance of ^{20}Ne and ^{16}O . At TAMS (*solid* lines), where most of the central hydrogen has been processed ($f_{\text{H}} = 0.99$), a depletion in ^{16}O abundance is also observed. At this late stage, there is also a secondary increase in ^{14}N in the core of the star.

In summary, we see that ^1H , ^4He and ^{16}O abundances evolve gradually, slowly extending to larger parts of the star and encompassing larger radii, while ^{12}C and ^{14}N abundances evolve rapidly across the burning region. All stars follow a similar trend. The most massive star in this study ($3M_{\odot}$) has, at TAMS, large compositional changes across roughly half of its mass (or about 20% of its radius). As discussed by [4], in the fallback material from a TDE we expect ^{12}C and ^{14}N abundance anomalies to be more noticeable and appear at earlier times than the other elemental anomalies.

As a star evolves along the MS, its average density, $\bar{\rho}_{\star}$, decreases and its core density, ρ_{core} , increases (see Section 2.1). This is illustrated in Figure 3.4, where we show the evolution of the

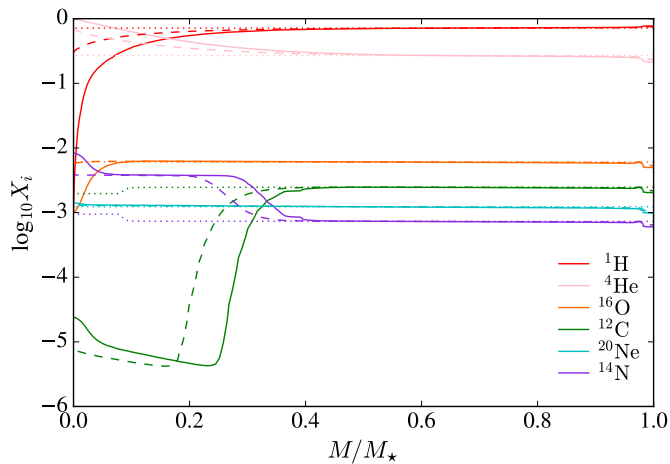


Figure 3.3: Compositional abundance as a function of enclosed mass in a $1M_{\odot}$ star at three different evolutionary stages during its MS lifetime. In this paper, we characterize evolutionary stages by f_{H} , the fraction of central hydrogen that has been burned. Here we show the stellar profiles for $f_{\text{H}} = 0.0 = f_{\text{ZAMS}}$ (*dotted*), $f_{\text{H}} = 0.60$ (*dashed*), and $f_{\text{H}} = 0.99$ (*solid*), respectively. A $1M_{\odot}$ star disrupted at later stages in its evolution should reveal abundance anomalies: an increase in nitrogen and depletion of oxygen, as previously argued by [4].

density profile for a $1M_{\odot}$ star with initial solar abundance from ZAMS to TAMS. Since the star’s radius increases with age while its mass remains nearly constant, $\bar{\rho}_{\star}$ decreases with age. The effects of $\bar{\rho}_{\star}$ on the star’s vulnerability to tidal deformations can be readily seen by rewriting r_{t} as

$$r_{\text{t}} \cong \left(\frac{M_{\text{bh}}}{\bar{\rho}_{\star}} \right)^{1/3}. \quad (3.4)$$

This scaling implies that as the star evolves, it becomes progressively more vulnerable to tidal deformations and mass loss. However, this scaling is unable to accurately capture the exact impact parameter required to fully disrupt a star. This is because as the star evolves a denser core, a surviving core is likely to persist for a disruption at r_{t} ($\beta = 1$), which is the penetration factor assumed for the analytical calculations. Nonetheless, we expect the time and magnitude of the peak accretion rate to be reasonably well captured by the simple formalism described here.

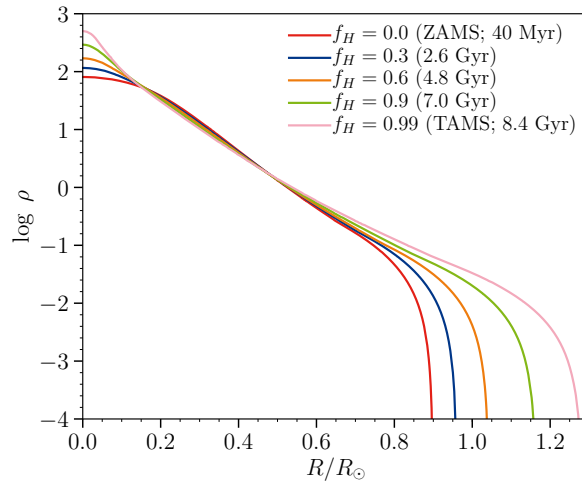


Figure 3.4: Density profiles for a $1M_{\odot}$ star at different times along its MS evolution. The *red* line corresponds to ZAMS with a central density of 81 g cm^{-3} and the *pink* line corresponds to a central hydrogen fraction of 10^{-3} with a central density of 500 g cm^{-3} . These different density profiles result in different r_t and thus exhibit different vulnerability to disruption.

4 The Disruption of Evolved MS Stars

4.1 Tidal Vulnerability

¹ Here we analyze how the tidal radius, $r_{t,\star}$, evolves with stellar mass and age along the MS for the stars in our study. The left panel of Figure 4.1 shows $r_{t,\star}$ normalized to the tidal radius of the same star at ZAMS, $r_{t,\text{ZAMS}}$. We plot this ratio as a function of f_{H} , the fraction of central hydrogen burned, and stellar mass M_{\star} . We find that the tidal radius increases with age and evolves more dramatically with f_{H} throughout the lifetime of more massive stars. For example, the tidal radius of a $3M_{\odot}$ star increases by roughly a factor of two over its MS lifetime. This is because the average density of a more massive star increases faster, and by Equation 3.4, $r_t \propto \bar{\rho}_{\star}^{-1/3}$. This means that as stars move along the MS, they become progressively more vulnerable to tidal dissipation and mass stripping.

Next, we discuss how the vulnerability of regions with processed element abundances compares to that of the entire star. This region of the star is important as it will reveal characteristic composition features during the tidal disruption event. The right panel of Figure 4.1 shows the ratio of $r_{t,\star}$ to $r_{t,\text{burn}}$, where $r_{t,\text{burn}}$ is defined as the tidal radius of material within the regions of a star that exhibit active nuclear burning. This region of active nuclear burning is defined to be where the specific power from nuclear reactions is greater than $1 \text{ erg g}^{-1}\text{s}^{-1}$. This is a consistent way for defining the burning region throughout all of the stellar profiles calculated here. This region of active nuclear burning is located at small radii where the density is much higher than $\bar{\rho}_{\star}^{-1/3}$ and

¹Except for a few changes, this Chapter was taken from the publication.

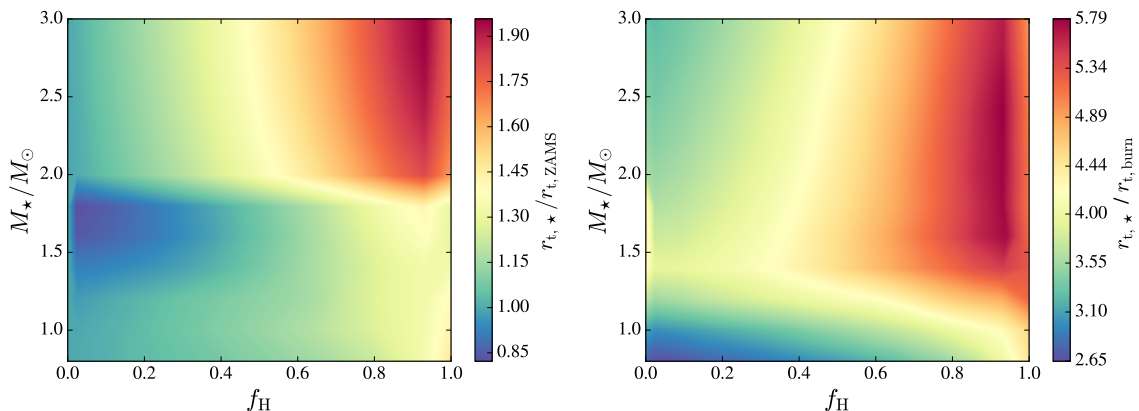


Figure 4.1: In both panels, the color scale shows the tidal radius of the disrupted star. *Left panel:* Plotted are the ratio of the star’s tidal radius to the tidal radius of that same star at ZAMS ($f_H = 0.0 = f_{\text{ZAMS}}$). This shows that the star’s vulnerability to disruption increases with age. This effect is stronger for more massive stars. *Right panel:* Plotted are the ratio of the tidal radius to $r_{\text{t,burn}}$. Here $r_{\text{t,burn}}$ is defined as the tidal radius of the star’s core undergoing active nuclear burning, where the specific power from nuclear reactions is greater than $1 \text{ erg g}^{-1}\text{s}^{-1}$. This shows that all of the stars in our study require deeper encounters to strip mass from their burning regions.

thus deeper penetrations are required in order to observe the evolved element abundances in the fallback material. Also, as this region is located within the innermost layers of the star, the processed elements will be revealed in the fallback material only at later times.

4.2 The Disruption of a Sun-like Star

In this section we begin the tidal disruption of a Sun-like star. Figure 4.2 shows the mass fallback rate arising from the full disruption at r_t of a $1M_\odot$ star at two different evolutionary states: at ZAMS (*dotted* lines) and after 4.8 Gyr (*dashed* lines), when more than half of the central hydrogen has been processed ($f_H = 0.60$). These curves are normalized to the peak fallback rate and peak time of the corresponding ZAMS star: $\dot{M}_{\text{peak,ZAMS}}$ and $t_{\text{peak,ZAMS}}$, respectively. The compositions of the stars before disruption are shown in Figure 3.3 as *dotted* (ZAMS) and *dashed* ($f_H = 0.60$) lines. The disruption of the TAMS $1M_\odot$ star, whose composition is shown by the *solid* lines in Figure 3.3, is expected to be similar in shape to the disruption of the $f_H = 0.60$ star, with an enhancement in ^{14}N and depletion in ^{12}C .

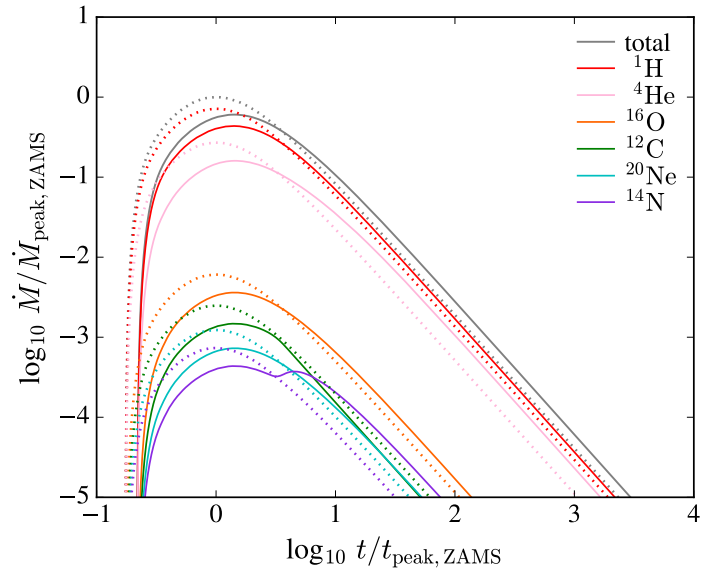


Figure 4.2: Mass fallback rates for elements that make up 99.6% of the mass of a $1M_{\odot}$ tidally disrupted star at two different evolutionary stages. The star aged nearly 5 Gyr from the *dotted* lines ($f_{\text{H}} = 0.0 = f_{\text{ZAMS}}$) to the *solid* lines ($f_{\text{H}} = 0.60$). \dot{M} for the total mass of the star is shown by the *gray* curves. All curves are normalized to \dot{M}_{peak} and t_{peak} for the corresponding ZAMS star. The main changes in fallback rates as the star evolves along the MS are an increase in nitrogen and a decrease in carbon after t_{peak} due to CNO activity in the core.

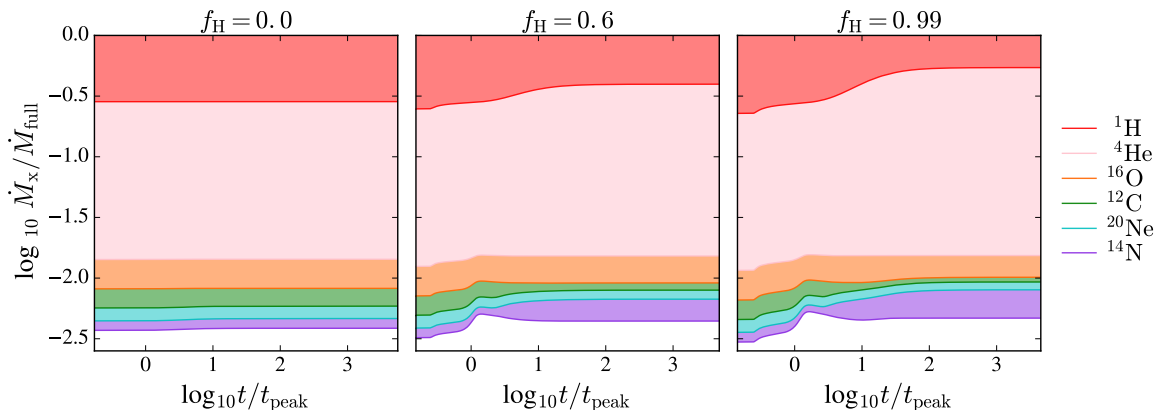


Figure 4.3: The fallback rate for different elements, \dot{M}_X , following the disruption of a $1M_{\odot}$ star at three different evolutionary stages. The *left* and *center* panels correspond to the *dotted* and *solid* lines shown in Figure 4.2, respectively. The *right* panel shows \dot{M} for the same star but at $f_{\text{H}} = 0.99$, which corresponds to an age of 8.3 Gyr. Time is in units of t_{peak} . As the star ages we see an increase in nitrogen and a decrease in carbon abundance but only after t_{peak} .

The smooth behavior of the fallback rates for all the plotted elements during the disruption of the ZAMS star (*dotted* lines in Figure 3.3) is the result of the nearly homogeneous elemental composition within the star. The fallback rates for the $f_{\text{H}} = 0.60$ star (*dashed* lines in Figure 3.3), on the other hand, contain information about the varying nature of its elemental composition. In the fallback rates we can see an obvious increase in ^{14}N , decrease in ^{12}C , and a slight increase in ^4He , which is consistent with the compositional structure of the star before disruption. These results are in agreement with previous studies [4]. We note that the fallback curves for the $f_{\text{H}} = 0.60$ star have no abundance variations at $t \lesssim t_{\text{peak}}$. These compositional anomalies might provide insight into the nature of the progenitor star near or after the most luminous time of the tidal disruption flare.

In Figure 4.3 we show the fractional contribution to the total fallback rate arising from each element during the disruption of a $1M_{\odot}$ star at three different evolutionary stages. From left to right, these panels correspond to the ZAMS (*dotted*), $f_{\text{H}} = 0.60$ (*dashed*), and TAMS (*solid*) composition profiles in Figure 3.3, respectively. In each panel we calculate the ratio of the fallback rate for each element, \dot{M}_X , to the total mass fallback rate, \dot{M}_{full} .

As a result, for the disruption of a $1M_{\odot}$ star, it might be challenging to distinguish its evolutionary stage using spectral information if it is only obtained at $t \lesssim t_{\text{peak}}$ (although the exact

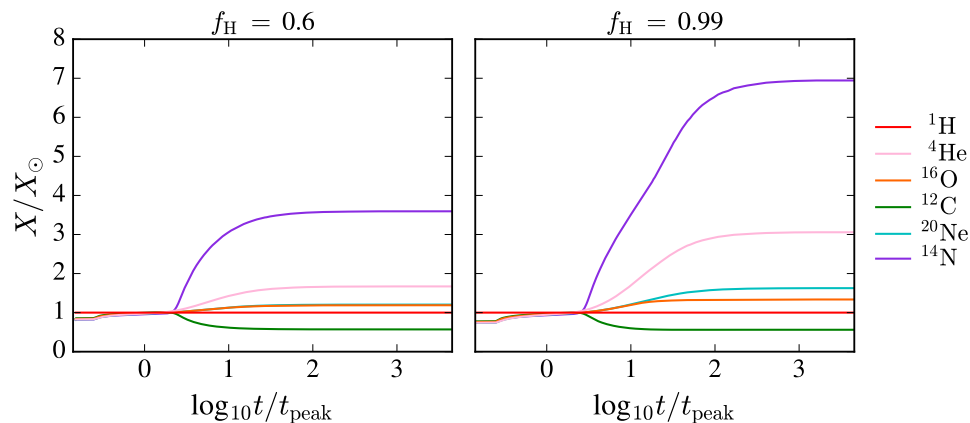


Figure 4.4: Elemental abundance of the fallback material relative to solar following the disruption of a $1M_{\odot}$ at two different evolutionary stages: $f_{\text{H}} = 0.60$ (*left* panel) and TAMS (*right* panel). A rapid evolution of ^{14}N and ^{12}C abundance relative to the other elements is clearly seen. The solar ratios clearly illustrate the significance of the variations in the abundances of ^{16}O , ^4He , and ^{20}Ne .

values of \dot{M}_{peak} and t_{peak} are expected to be distinct; Figure 4.8). This is, however, not the case after t_{peak} .

Figure 4.4 shows the abundance of the fallback material relative to solar following the disruption of a $1M_{\odot}$ at two different evolutionary stages: $f_{\text{H}} = 0.60$ (*left* panel) and TAMS (*right* panel). Elemental abundances relative to solar are calculated here using

$$\frac{X}{X_{\odot}} = \frac{\dot{M}_X/\dot{M}_{\text{H}}}{M_X/M_{\text{H},\odot}}, \quad (4.1)$$

where \dot{M}_X is the fallback rate for a selected element, \dot{M}_{H} is the fallback rate of ^1H , and $M_X/M_{\text{H},\odot}$ is the abundance mass ratio relative to solar of element X. The disruptions of a $f_{\text{H}} = 0.60$ and a TAMS star each show a significant increase in ^{14}N and ^4He after t_{peak} . As expected, these features are more prominent for the TAMS star. Near $t = 10t_{\text{peak}}$, Figure 4.4 shows steeper abundance gradients in the *right* panel compared to the *left* in all elements except ^{12}C . We note that these values are relative to ^1H . This is important in the case of ^{16}O and ^{20}Ne where we see an increase in their abundance. This is because while ^1H is depleted at every evolutionary stage, ^{16}O and ^{20}Ne abundance remain relatively constant for a star of this mass, which results in higher solar ratios. However, this behavior is also altered by the mass of the star as we discuss in the following section.

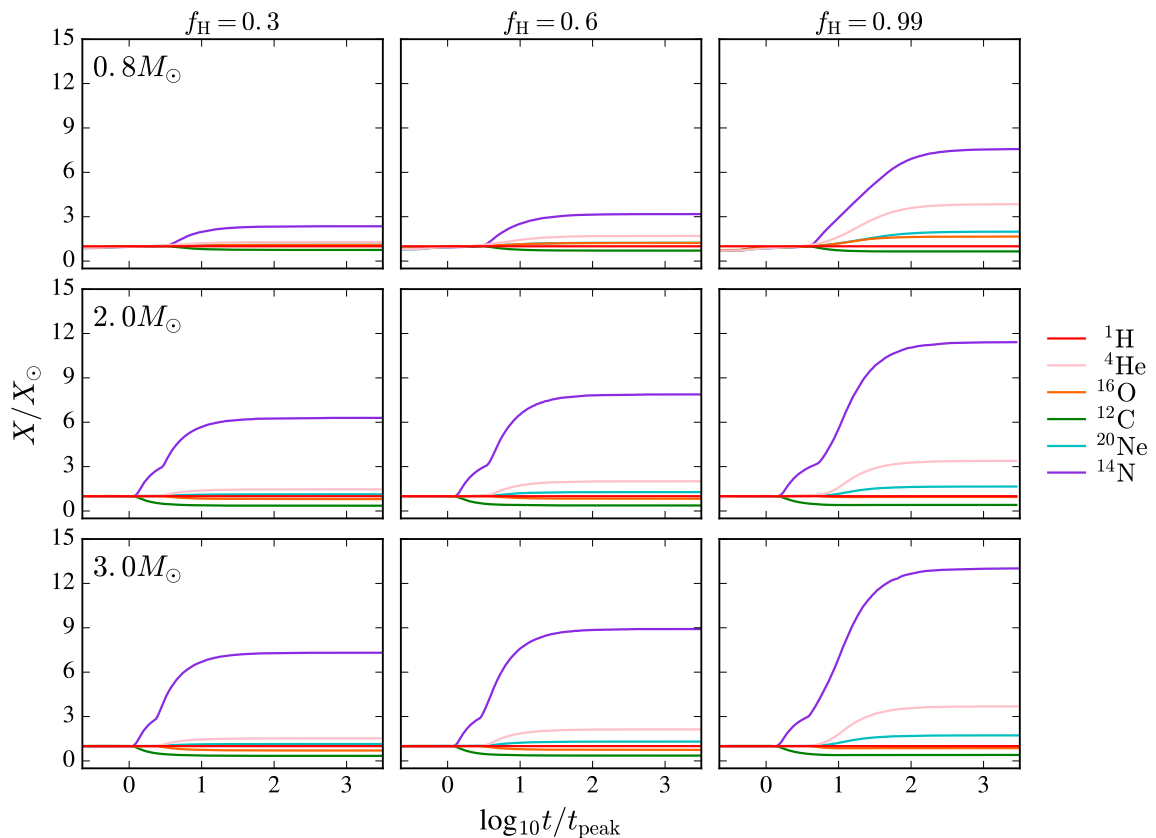


Figure 4.5: The relative abundance of stellar debris as a function of fallback time arising from the disruption of $0.8M_{\odot}$ (top row), $2.0M_{\odot}$ (middle row) and $3.0M_{\odot}$ (bottom row) stars at three different evolutionary stages ($f_{\text{H}} = 0.3, 0.6$ and 0.99). The change in abundance relative to solar is observed to increase with mass and age but only after t_{peak} . These anomalies appear at earlier times for higher mass stars.

4.3 Disruption of MS stars

For reasons discussed previously, it seems likely that the evolutionary state of a star might be revealed by charting the compositional evolution of the fallback material, which might be inferred from particular features in the spectra of the resulting luminous flare. The association of a significant fraction of TDEs with galaxies that are no longer forming stars [9, 32, 33, 34] has suggested the likely presence of evolved stars in the nuclei of TDE hosts, or at least a subset thereof. Much of our effort in this section will thus be dedicated to determining the state of the fallback material after the tidal disruption of stars of a wide range of ages and masses.

In Figure 4.5 we show the relative abundances of the fallback material for three representative MS star disruptions. The *first row* of panels shows the abundance of the fallback material for a $0.8M_{\odot}$ star tidally disrupted at three different evolutionary stages: $f_{\text{H}} = 0.3$, $f_{\text{H}} = 0.6$, and $f_{\text{H}} = 0.99$. The abundances shown are similar to those shown in Figure 4.4 for a $1M_{\odot}$ star. At these low masses, we expect the abundance anomalies to be present in the fallback material at a few times t_{peak} .

The *second row* of panels in Figure 4.5 shows the relative abundances of the fallback material for a disrupted $2M_{\odot}$ star. The abundance patterns are broadly similar to those seen for the $0.8M_{\odot}$ and $1M_{\odot}$ stellar disruptions. However, there are three main differences. First, in contrast to the observed increase of ^{16}O seen in the $0.8M_{\odot}$ and $1.0M_{\odot}$ disruptions, a significant decrease in ^{16}O abundance is observed. This is an indication of the increased CNO activity in the $2M_{\odot}$ star. Second, two distinct bumps are seen in the evolution of the ^{14}N abundance, contrary to its steady increase in the smaller mass disruptions. The first increase in ^{14}N abundance (and the corresponding ^{12}C depletion) is due to the local maximum of CNO burning that is located at roughly 20% of the star's radius. There is also significant CNO and p-p chain activity in the star's core, which is revealed at later times in the fallback material, and leads to the relatively delayed increase in ^4He and ^{20}Ne , the corresponding decrease of ^{16}O , and a secondary increase in ^{14}N . Third, abundance variations are observed significantly closer to t_{peak} in the $2M_{\odot}$ disruptions than in the $0.8M_{\odot}$ disruptions. This is a result of the more extended burning region within the star, whose material is revealed at earlier times following the disruption.

In the *bottom row* of panels in Figure 4.5 we show the composition of the fallback material following the disruption of a $3M_{\odot}$ star. The abundance variations in these fallback curves closely resemble those for the $2M_{\odot}$ star, but with larger variations appearing at earlier times. The abundance variations presented in Figure 4.5 for the few representative stars accurately describe the overall trends in our sample. These trends are illustrated in Figure 4.6, in which various elemental abundances are shown at the time that the mass fallback rate has reached one tenth of its peak

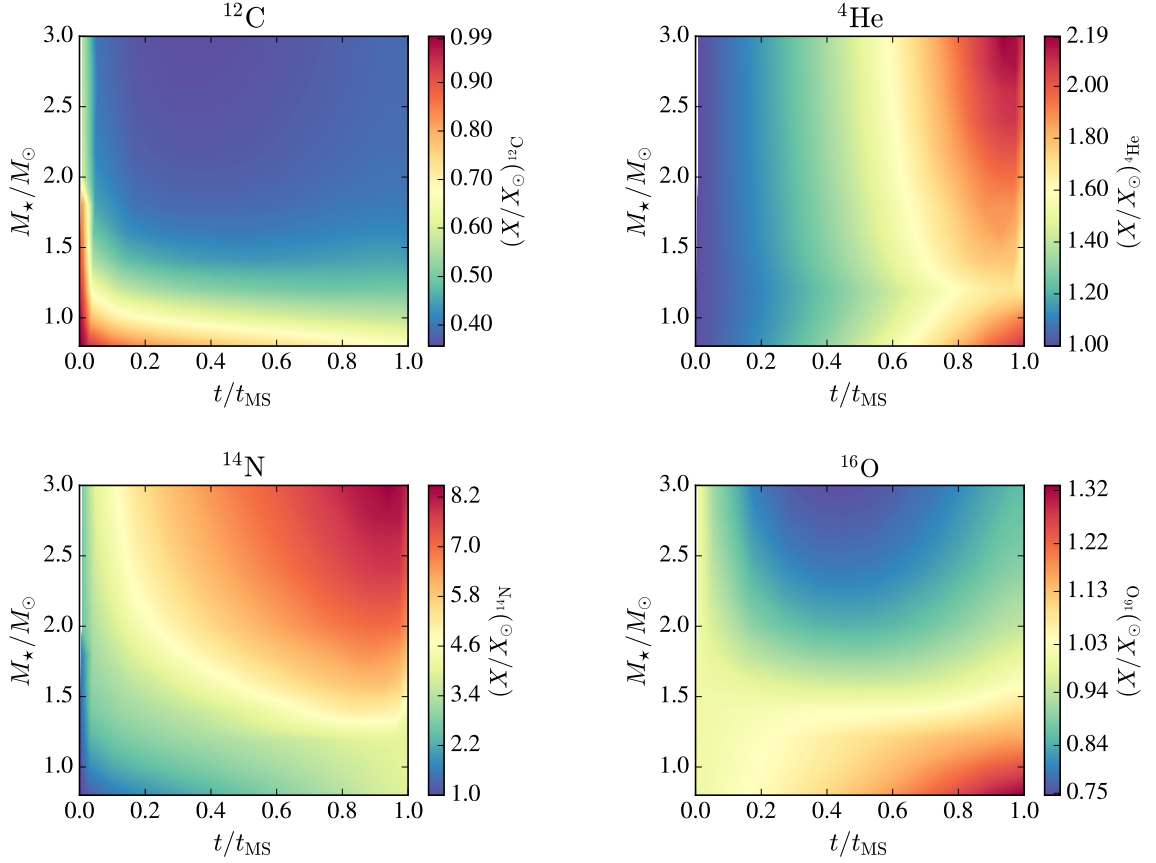


Figure 4.6: Elemental abundances relative to solar at the time the mass fallback rate has reached one tenth of its peak value, $t_{0.1} > t_{\text{peak}}$, for all of the stellar masses and ages in our sample. Elements of interest are ^{12}C , ^4He , ^{14}N and ^{16}O . Values are shown as a function of the star’s fractional main sequence lifetime and stellar mass. We find carbon abundances to be more indicative of stellar mass for $M_* \lesssim 1.5M_\odot$, while helium abundances are correlated with stellar age for all masses. $(X/X_\odot)_{^{14}\text{N}} \gtrsim 5.0$ occurs only for masses greater than $1.5M_\odot$ and develops early in the star’s evolution. We also find oxygen abundances to be primarily stellar mass dependent.

value, $t_{0.1} > t_{\text{peak}}$.

The fallback abundances at $t_{0.1}$ are plotted in Figure 4.6 as a function of the star’s fractional main sequence lifetime, t/t_{MS} , and stellar mass. In Figure 4.7 we show the same abundance values as in Figure 4.6 but presented with the evolutionary age of the star in years. Some key points should be emphasized. We find carbon decrements to be indicative of stellar mass, while helium enhancements are indicative of age. $(X/X_\odot)_{^{14}\text{N}} \gtrsim 5.0$ occurs only for masses greater than $1.5M_\odot$ and develops early in the star’s evolution. This is due to the enhanced CNO activity inside the more massive stars in our sample. We also find oxygen abundances to be primarily dependent on stellar mass.

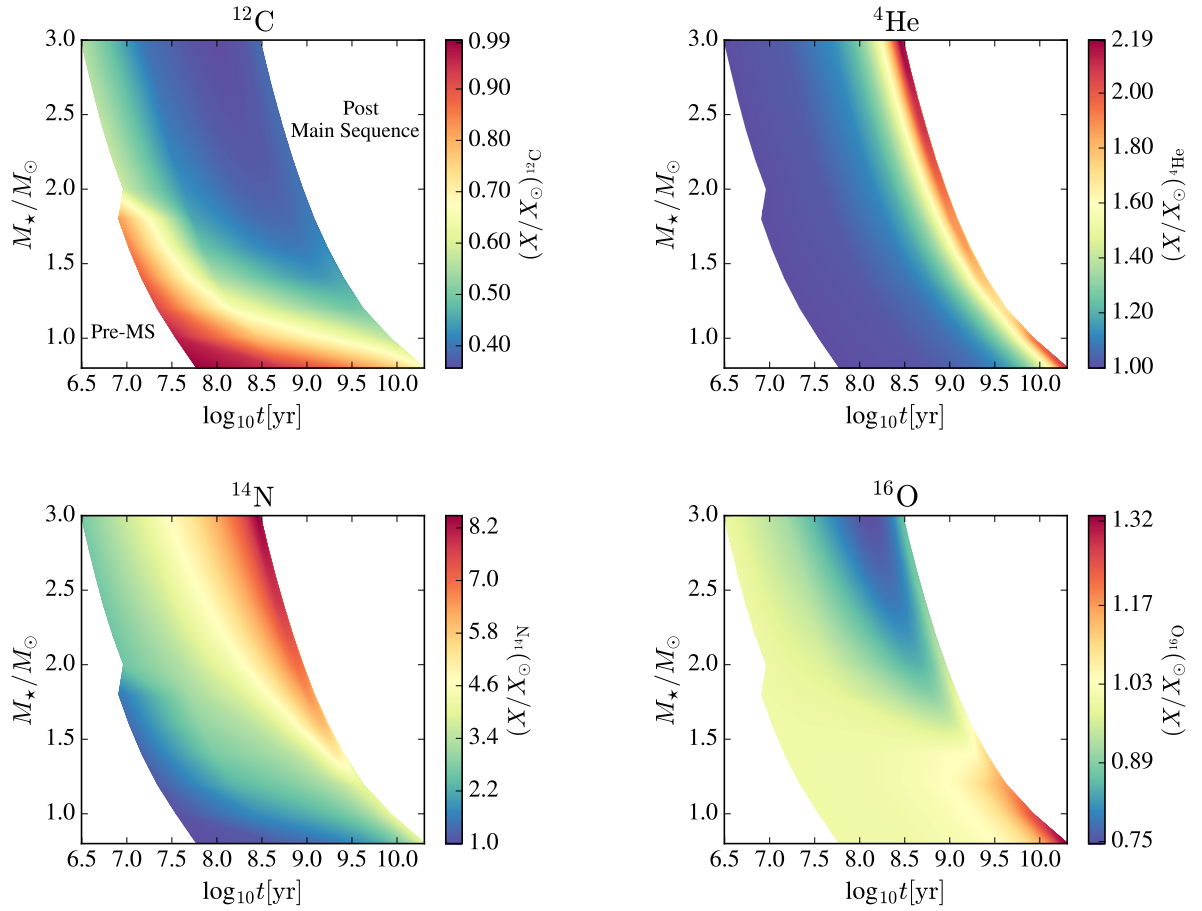


Figure 4.7: Same as Figure 4.6 but presented with stellar age in years (x -axis). The white regions correspond to pre-MS (*left*) or post-MS (*right*).

The processes discussed here suggest that TDEs may have a more complex spectrum and time-structure than simple models suggest. The effects are especially interesting when the accretion rate is high, as this gives rise to high luminosities, and thus can more readily offer clues to the nature of the disrupted star. The specific values of \dot{M}_{peak} and t_{peak} can further aid in distinguishing the properties of the progenitor star before disruption. This is illustrated in Figure 4.8 where we show abundances of carbon, helium, nitrogen and oxygen (relative to solar) in the fallback debris as a function of \dot{M}_{peak} and t_{peak} . Each panel in Figure 4.8 corresponds to a different element, the different lines correspond to different stars in our study ($0.8M_{\odot}$, $1.0M_{\odot}$, $1.2M_{\odot}$, $1.4M_{\odot}$, $2.0M_{\odot}$, and $3.0M_{\odot}$), the points are different stages in the stars' evolution on the MS (roughly equally spaced in time), and the color of the points is the abundance of the fallback debris at the time that \dot{M} falls to one tenth of its peak value, $t_{0.1}$. We used the fitting formulas presented in [3], which give \dot{M}_{peak} and t_{peak} given β , γ , M_{\star} , and R_{\star} . We used $\gamma = 4/3$ and its corresponding penetration factor for full disruption ($\beta = 1.85$) given by [3]. The values of M_{\star} and R_{\star} were taken from the MESA profiles and we have assumed $M_{\text{bh}} = 10^6 M_{\odot}$ (the reader is referred to equations 3.2 and 3.3 for the scalings of \dot{M}_{peak} and t_{peak} with M_{bh} , respectively). The abundance values are the same as in Figure 4.6.

The variation in elemental abundances is accompanied by a wide range in \dot{M}_{peak} and a moderate range in t_{peak} ; a combination of these different pieces of information can help characterize the progenitor stars of TDEs. For example, the disruption of a $3M_{\odot}$ star has similar t_{peak} values to that of a $2M_{\odot}$ star. While their ^{12}C and ^{16}O abundances are very similar, the $3M_{\odot}$ star's disruption results in a higher abundance in ^{14}N and ^4He at every stage in its evolution, along with a higher \dot{M}_{peak} . In the lower mass stars ($0.8\text{--}1.4M_{\odot}$) there are many degeneracies in \dot{M}_{peak} and t_{peak} values. Here, the ^{14}N , ^{16}O , and ^4He abundances are similar (over the age of the universe) but the ^{12}C abundances vary at the early stages in these stars' MS evolution. Compositional information, combined with reprocessing and radiative transfer calculations (e.g. [17]), can thus be used to discern the stellar mass and age of the disrupted star.

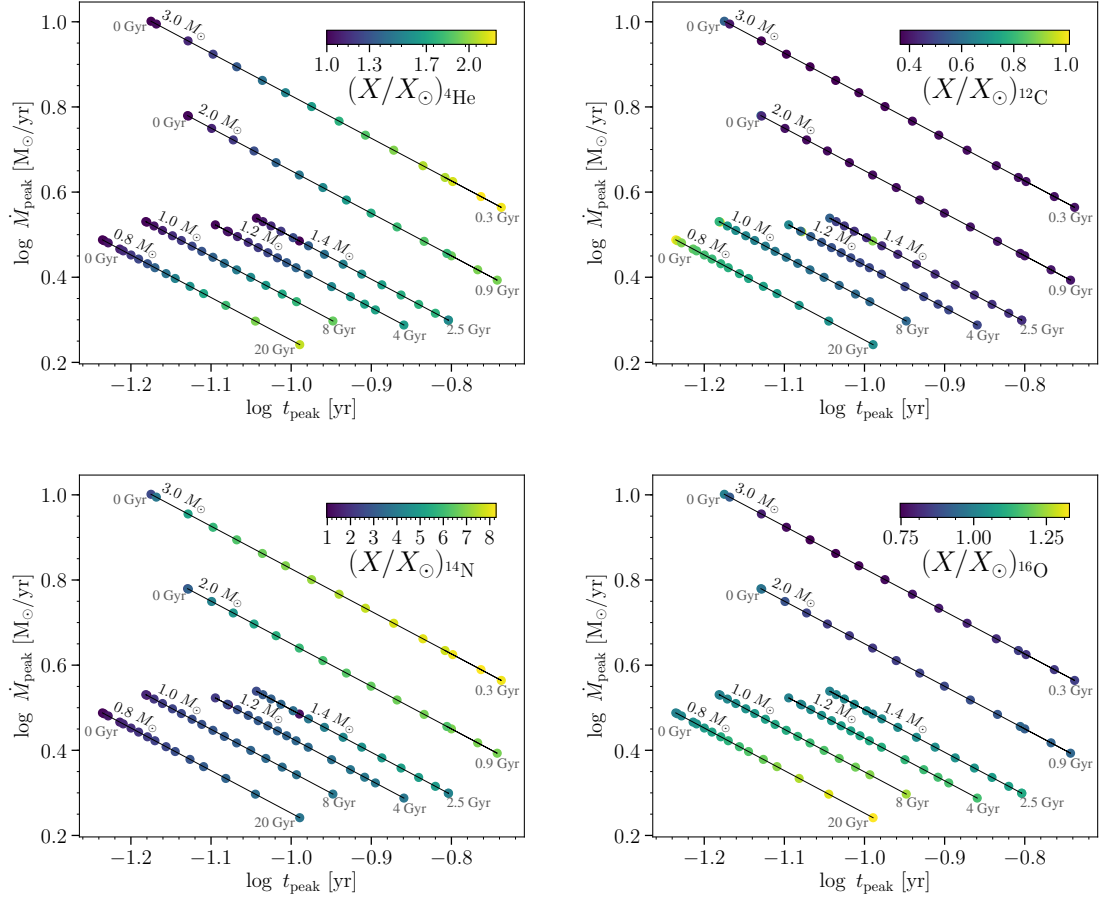


Figure 4.8: Fallback abundance at $t_{0.1}$ of ${}^4\text{He}$, ${}^{12}\text{C}$, ${}^{14}\text{N}$, and ${}^{16}\text{O}$ (clockwise from top left) for the disruption (by a $M_{\text{bh}} = 10^6 M_{\odot}$ SMBH) of $0.8 M_{\odot}$, $1 M_{\odot}$, $1.2 M_{\odot}$, $1.4 M_{\odot}$, $2.0 M_{\odot}$, and $3.0 M_{\odot}$ stars along their MS evolution. Abundances are at $t_{0.1}$, but points are placed at \dot{M}_{peak} and t_{peak} for the disruption of each star. Abundances are quoted relative to solar. Points are roughly equally spaced in time for each mass, with the top-left-most point being ZAMS and the bottom-right-most point being TAMS. (This is not strictly true for the ZAMS point of the $1 M_{\odot}$, $1.2 M_{\odot}$, and $1.4 M_{\odot}$ stars as their radius slightly decreases at the very beginning of their MESA evolution, but all other points for these stars proceed left to right with age as the star subsequently evolves.)

5 Discussion

5.1 Summary of Key Results

¹ Motivated by previous work, we have modeled the tidal disruption of MS stars of varying mass and age. We adopted an analytic formalism to study the time evolution of the composition of the fallback debris onto the SMBH. We compared the analytic method to hydrodynamic simulations in Figure 3.2 and found, similarly to [27] and [31], that the broad features of the fallback curves are reasonably well captured by it.² Using the analytic formalism, we quantify the variations in composition arising from the disruption of 12 different stars with masses of $0.8\text{--}3.0M_{\odot}$ at 16 different evolutionary stages along the MS. The main results of our study are the following.

1. We predict an increase in nitrogen and depletion in carbon abundance in the fallback debris with MS evolution for all stars in our sample, which is in agreement with previous studies [4]. We find a decrease in oxygen with MS evolution for $M_{\star} \gtrsim 1.5M_{\odot}$, and an increase for $M_{\star} < 1.5M_{\odot}$.
2. For all of the TDEs modeled in this study, we find that the time during the fallback rate curve when anomalous abundance features are present, t_{burn} , is *after* the time of time of peak fallback rate t_{peak} .
3. Abundance variations are more significant and $t_{\text{burn}}/t_{\text{peak}}$ is smaller for stars of larger mass.

¹Except for a few changes, this Chapter was taken from the publication.

²This work should, however, be taken only as a guide for the expected compositional trends in the fallback material, as hydrodynamical simulations are needed to accurately predict the evolution and characteristics of the flares.

4. Some key variations in the compositional evolution are highlighted, along with the types of observation that would help to discriminate between different stellar disruptions. In particular, we find carbon and oxygen abundances to strongly dependent on stellar mass for $M_\star \lesssim 2M_\odot$, while helium abundances are found to be correlated with stellar age for all masses. $(X/X_\odot)_{^{14}\text{N}} \gtrsim 5.0$ occurs only for masses greater than $1.5M_\odot$ and is observed early in the star’s evolution.
5. Studying the compositional variation in the fallback debris provides a clear method for inferring the properties of the progenitor star before disruption.

5.2 Implications for Observations and Models

It is evident from the results described above that the evolution of the interior structure of stars during their MS lifetimes is very rich. Even in the simplest case of a Sun-like star, complex behavior with multiple abundance transitions in the fallback material may be observed. The resulting TDE spectra are expected to depend fairly strongly on the abundance properties of the fallback material [17]. This implies that if one can be very specific about the times at which we expect to see such spectral features in the observed emission of the tidal disruption event, one can better constrain the properties of the disrupted star.

Motivated by this, in Figure 5.1 we plot the fallback time t_{burn} , relative to t_{peak} , at which we expect to see anomalous abundance variations. Here t_{burn} is defined as the time at which the abundances of ^{12}C and ^{14}N in the fallback material, as presented in Figures 4.4 and 4.5, both deviate from unity. $t_{\text{burn}}/t_{\text{peak}}$ is shown in Figure 5.1 as a function of stellar mass and age (characterized by f_{H}). At fixed values of f_{H} we see that non-solar abundances in the fallback debris begin to appear systemically closer to t_{peak} as stellar mass increases. For the $3.0M_\odot$ star, $t_{\text{burn}} \approx 1.2t_{\text{peak}}$ for $f_{\text{H}} \lesssim 0.3$. For constant M_\star , $t_{\text{burn}}/t_{\text{peak}}$ increases mildly with f_{H} for stars with $M_\star > 1.6M_\odot$. For stars with $M_\star < 1.6M_\odot$, this ratio remains fairly constant throughout the star’s evolution. In summary, t_{burn} depends strongly on M_\star but has a relatively weak dependence on stellar age. It

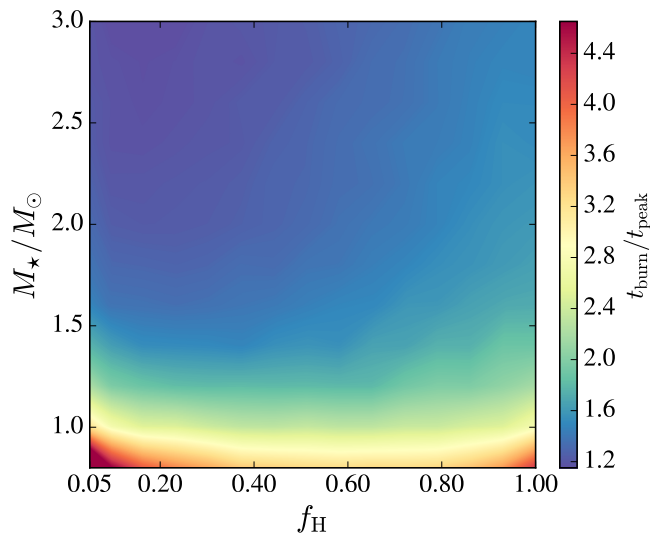


Figure 5.1: The ratio of t_{burn} to t_{peak} as a function of f_{H} and stellar mass. Here t_{burn} is the time when non-solar abundance ratios begin to appear in the fallback material, specifically when the abundance of ^{12}C and ^{14}N deviate from solar. We have explicitly excluded $f_{\text{H}} \lesssim 0.05$ from this plot, given that these stars experience some mild contraction early in their MESA evolution. The ratio ($t_{\text{burn}}/t_{\text{peak}}$) reaches a maximum (minimum) value of 7.6 (1.15) for a $0.8M_{\odot}$ ($3M_{\odot}$) star at $f_{\text{H}} = 0.05$ ($f_{\text{H}} = 0.23$).

is important to note that independently of the mass and age of the disrupted star, no anomalous abundances are expected to be observed before t_{peak} .

Information regarding the nature of the disrupted star should be imprinted on the properties of the TDE light curve (e.g., t_{peak} and \dot{M}_{peak}) and spectrum (particularly at $t \gtrsim t_{\text{burn}}$). Current observations of TDEs show clear differences in their rise and decay properties as well as in their spectral evolution. Peculiar emission features have been observed in their spectra, which include an array of helium, hydrogen, and nitrogen broad line emission features. The origin of these features as well as their associated line ratios have caused significant debate. The extreme helium to hydrogen line ratio observed in the transient event PS1-10jh was initially proposed to be the result of the tidal disruption of a helium-rich star [11]. However, such line ratios have also been shown to arise from the reprocessing of radiation through the fallback debris of a disrupted Sun-like star [17]. As for the additional presence of rare nitrogen features, [4] first proposed that the disruption of MS stars with evolved stellar compositions could lead to enhanced nitrogen (as well as anomalous helium and

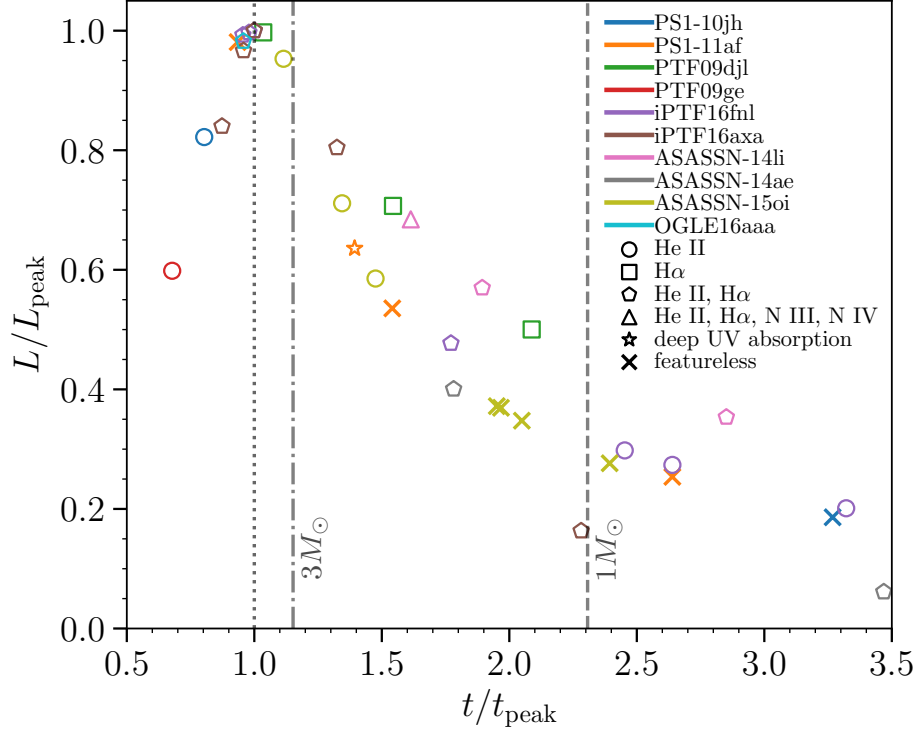


Figure 5.2: Compositional features in the spectra of well-sampled tidal disruption events with existing spectroscopic observations. The y - and x -axes show luminosity and time relative to peak respectively, with different colors corresponding to distinct events, and different symbols corresponding to different spectral features. We show the minimum values of $t_{\text{burn}}/t_{\text{peak}}$ (Figure 5.1) as derived from our study for a $1M_{\odot}$ (dashed line) and $3M_{\odot}$ (dash-dotted line) star.

carbon abundances).

In Figure 5.2, we show compositional features in the spectra of ten observed TDEs. We place each spectrum in the light curve of each event, relative to its peak luminosity and peak time. The TDE luminosity curve fits of the observed data for each event were generated by [35]. Symbols indicate features present in the spectra. Data for the spectral features is taken from [11, 36, 37, 9, 15, 38, 39, 40, 10, 16, 18, 14, 13, 12].

Several TDE spectra show compositional features at or near the peak in their light curve. Our calculations (in particular see Section 4.3 and Figure 5.1) predict no compositional abundance changes (relative to solar) in the fallback material at or near peak due to the star. This implies that

the strong helium to hydrogen line ratios should occur even at solar composition, as argued by [17]. For observations at $t > t_{\text{burn}}$, we expect the reprocessing material to be enhanced in helium, yet the optical depth effects are expected to be less important [41]. As such, radiation transfer calculations are needed before firm conclusions can be derived from observations of evolving line ratios in a given TDE.

Nitrogen emission lines, on the other hand, are only currently detected at $t \gtrsim 1.2t_{\text{peak}}$. If their presence is attributed to a drastic increase in nitrogen abundance, then based on the results shown in Figures 4.8 and 5.1, one would conclude that $M_{\star} \gtrsim 1.8M_{\odot}$ for the star whose disruption triggered the ASASSN-14li flaring event and $M_{\star} \gtrsim 3.0M_{\odot}$ for the star whose disruption triggered iPTF16fnl. However, early spectra that show a lack of nitrogen emission lines at early times are needed to support constraints such as these. With this we see that the timescale for chemical enrichment (i.e., t_{burn}) can thus provide a direct observational test of which stars are being disrupted by the central SMBH.

Much progress has been made in understanding how the feeding rate onto a SMBH proceeds after the disruption of a particular star, and in deriving the properties of the flares that follow from this. There still remain a number of mysteries, especially concerning the identity of the star, the nature of the energy dissipation mechanism, and the time scales involved. The class of models we have presented here predict that the spectral properties of the fading signals will turn out to be even more telling and fascinating than initially anticipated.

Future work will include a more detailed exploration of the parameters governing the abundance of the fallback material, including hydrodynamical calculations [19] as well as radiative transfer calculations [17] evolved over time for different properties of the reprocessing material. Studies of this sort, in comparison with improved spectral observations of TDEs, will undoubtedly help clarify the physics governing these transient sources.

Bibliography

- [1] M. J. Rees, *Nature*, **333**, 523 (1988).
- [2] M. A. G. Jethro Andal, Illustration of accretion onto a SMBH, futurism.com/all-about-black-holes/.
- [3] J. Guillochon and E. Ramirez-Ruiz, *ApJ*, **767**, 25 (2013).
- [4] C. S. Kochanek, *MNRAS*, **458**, 127 (2016).
- [5] J. Frank and M. J. Rees, *MNRAS*, **176**, 633 (1976).
- [6] M. Kesden, in *Tidal Disruption by Spinning Supermassive Black Holes* (SnowPAC 2013, Utah, 2013), p. 25.
- [7] M. MacLeod, J. Guillochon, and E. Ramirez-Ruiz, *ApJ*, **757**, 134 (2012).
- [8] K. Auchettl, J. Guillochon, and E. Ramirez-Ruiz, *ApJ*, **838**, 149 (2017).
- [9] I. Arcavi *et al.*, *ApJ*, **793**, 38 (2014).
- [10] T. W.-S. Holoiien *et al.*, *MNRAS*, **463**, 3813 (2016).
- [11] S. Gezari *et al.*, *Nature*, **485**, 217 (2012).
- [12] L. Wyrzykowski *et al.*, *MNRAS*, **465**, L114 (2017).
- [13] J. S. Brown, T. W.-S. Holoiien, K. Auchettl, K. Z. Stanek, C. S. Kochanek, B. J. Shappee, J. L. Prieto, and D. Grupe, *MNRAS*, **466**, 4904 (2017).

- [14] J. S. Brown, B. J. Shappee, T. W.-S. Holoiien, K. Z. Stanek, C. S. Kochanek, and J. L. Prieto, *MNRAS*, **462**, 3993 (2016).
- [15] J. S. Brown *et al.*, *MNRAS*, **473**, 1130 (2018).
- [16] T. W.-S. Holoiien *et al.*, *MNRAS*, **455**, 2918 (2016).
- [17] N. Roth, D. Kasen, J. Guillochon, and E. Ramirez-Ruiz, *ApJ*, **827**, 3 (2016).
- [18] S. B. Cenko *et al.*, *ApJL*, **818**, L32 (2016).
- [19] J. Law-Smith, M. MacLeod, J. Guillochon, P. Macias, and E. Ramirez-Ruiz, *ApJ*, **841**, 132 (2017).
- [20] B. Paxton, L. Bildsten, A. Dotter, F. Herwig, P. Lesaffre, and F. Timmes, *ApJS*, **192**, 3 (2011).
- [21] R. Kippenhahn, A. Weigert, and A. Weiss, *Stellar Structure and Evolution: , Astronomy and Astrophysics Library, 2012* (Springer-Verlag Berlin Heidelberg, Dordrecht, London, 2012).
- [22] A. C. Phillips, *The Physics of Stars* (PUBLISHER, ADDRESS, 1999).
- [23] J. Guillochon and E. Ramirez-Ruiz, *ApJ*, **809**, 166 (2015).
- [24] K. Hayasaki, N. Stone, and A. Loeb, *MNRAS*, **461**, 3760 (2016).
- [25] C. Bonnerot, E. M. Rossi, G. Lodato, and D. J. Price, *MNRAS*, **455**, 2253 (2016).
- [26] H. Shiokawa, J. H. Krolik, R. M. Cheng, T. Piran, and S. C. Noble, *ApJ*, **804**, 85 (2015).
- [27] G. Lodato, A. R. King, and J. E. Pringle, *MNRAS*, **392**, 332 (2009).
- [28] E. Ramirez-Ruiz and S. Rosswog, *ApJL*, **697**, L77 (2009).
- [29] P. Laguna, W. A. Miller, W. H. Zurek, and M. B. Davies, *ApJL*, **410**, L83 (1993).
- [30] J. Guillochon, E. Ramirez-Ruiz, S. Rosswog, and D. Kasen, *ApJ*, **705**, 844 (2009).
- [31] M. Kesden, *PhRvD*, **86**, 064026 (2012).



- [32] K. D. French, I. Arcavi, and A. Zabludoff, *ApJL*, **818**, L21 (2016).
- [33] K. D. French, I. Arcavi, and A. Zabludoff, *ApJ*, **835**, 176 (2017).
- [34] J. Law-Smith, E. Ramirez-Ruiz, S. L. Ellison, and R. J. Foley, *ApJ*, **850**, 22 (2017).
- [35] B. Mockler, J. Guillochon, and E. Ramirez-Ruiz, *ArXiv e-prints arXiv:1801.08221* (2018).
- [36] S. Gezari, R. Chornock, A. Lawrence, A. Rest, D. O. Jones, E. Berger, P. M. Challis, and G. Narayan, *ApJL*, **815**, L5 (2015).
- [37] R. Chornock *et al.*, *ApJ*, **780**, 44 (2014).
- [38] N. Blagorodnova *et al.*, *ApJ*, **844**, 46 (2017).
- [39] T. Hung *et al.*, *ApJ*, **842**, 29 (2017).
- [40] T. W.-S. Holoiien *et al.*, *MNRAS*, **445**, 3263 (2014).
- [41] J. Guillochon, H. Manukian, and E. Ramirez-Ruiz, *ApJ*, **783**, 23 (2014).

6 Appendix

6.1 Publication



Tidal Disruptions of Main-sequence Stars of Varying Mass and Age: Inferences from the Composition of the Fallback Material

Monica Gallegos-García¹, Jamie Law-Smith^{1,2} , and Enrico Ramirez-Ruiz^{1,2} 

¹Department of Astronomy and Astrophysics, University of California, Santa Cruz, CA 95064, USA; mpgalleg@ucsc.edu

²Niels Bohr Institute, University of Copenhagen, Blegdamsvej 17, DK-2100 Copenhagen, Denmark

Received 2018 January 10; revised 2018 March 5; accepted 2018 March 7; published 2018 April 20

Abstract

We use a simple framework to calculate the time evolution of the composition of the fallback material onto a supermassive black hole arising from the tidal disruption of main-sequence stars. We study stars with masses between 0.8 and $3.0 M_{\odot}$, at evolutionary stages from zero-age main sequence to terminal-age main sequence, built using the Modules for Experiments in Stellar Astrophysics code. We show that most stars develop enhancements in nitrogen (^{14}N) and depletions in carbon (^{12}C) and oxygen (^{16}O) over their lifetimes, and that these features are more pronounced for higher mass stars. We find that, in an accretion-powered tidal disruption flare, these features become prominent only after the time of peak of the fallback rate and appear at earlier times for stars of increasing mass. We postulate that no severe compositional changes resulting from the fallback material should be expected near peak for a wide range of stellar masses and, as such, are unable to explain the extreme helium-to-hydrogen line ratios observed in some TDEs. On the other hand, the resulting compositional changes could help explain the presence of nitrogen-rich features, which are currently only detected after peak. When combined with the shape of the light curve, the time evolution of the composition of the fallback material provides a clear method to help constrain the nature of the disrupted star. This will enable a better characterization of the event by helping break the degeneracy between the mass of the star and the mass of the black hole when fitting tidal disruption light curves.

Key words: black hole physics – galaxies: active – galaxies: nuclei – gravitation – stars: abundances

1. Introduction

Tidal disruption events (TDEs) offer a way to study both galactic supermassive black holes (SMBHs) and the dense stellar clusters that surround them. In these clusters, each star traces a complicated orbit under the combined influence of the SMBH and all the other stars. The orbits slowly diffuse as a result of the cumulative effect of stellar encounters (Magorrian & Tremaine 1999). There is a chance that one of these interactions will rapidly shift a star onto a nearly radial orbit, bringing it close to the SMBH. If a star wanders too close to the SMBH it can be violently ripped apart by the SMBH's tidal field (e.g., Rees 1988). As a result, for a full disruption, about half of the disrupted material eventually falls back and accretes onto the SMBH. This accretion is expected to power a flare that contains vital information about the disruption and can be used to constrain the properties of the SMBH and the disrupted object (Frank & Rees 1976).

The disruption of stars by SMBHs has been linked to tens of flares in the cores of previously quiescent galaxies (Komossa 2015; Aucht et al. 2017). Transient surveys such as the Palomar Transient Factory (PTF), the All-sky Automated Survey for Supernovae (ASAS-SN), and the Panoramic Survey Telescope and Rapid Response System (Pan-STARRS) are now finding increasing numbers of these events, especially at early times (Gezari et al. 2012; Arcavi et al. 2014; Holoien et al. 2014). By capturing the rise, peak, and decay of the flares, and with the addition of spectroscopic information, these events are starting to provide significant information about the underlying mechanisms (e.g., Guillochon et al. 2014).

Modeling TDEs properly requires a prediction of the rate of mass return to the SMBH after a disruption. While previous numerical results have provided reasonably precise models for the fallback resulting from the disruption of stars (e.g.,

Guillochon & Ramirez-Ruiz 2013), they are incomplete in that they do not directly examine the predicted compositional changes.³ Additionally, many previous studies have focused on stars of a single structural profile, usually selected to match the Sun. However, typical stellar mass functions in TDE host galaxies predict that tidal disruptions should commonly involve evolved main-sequence stars (Arcavi et al. 2014; French et al. 2016, 2017; Graur et al. 2018; Law-Smith et al. 2017b) whose internal structures are very diverse.

Given that the accretion time is inferred to be significantly shorter than the period of the returning debris in most events, the fallback rate is expected to track the flare luminosity relatively closely (Evans & Kochanek 1989; Ramirez-Ruiz & Rosswog 2009; Strubbe & Quataert 2009; Guillochon et al. 2014). As the number of observed disruptions increases, and as the cadence and quality of data continues to improve, it has become increasingly important to improve models of the fallback material for disruptions of all kinds.

The presence or absence of particular emission line features in the spectra of TDEs might be used as a probe of the nature of the disrupted star (Cenko et al. 2012; Gezari et al. 2012; Saxton et al. 2012; Arcavi et al. 2014; Holoien et al. 2014; Brown et al. 2015, 2016, 2017, 2018; Merloni et al. 2015; Cenko et al. 2016; Holoien et al. 2016a, 2016b; Leloudas et al. 2016; Wyrzykowski et al. 2017). Motivated by this, in this paper, we expand upon work by Kochanek (2016) to further characterize the rate of fallback and, in particular, the composition of the fallback debris. Our results predict what happens when stars of different masses and evolutionary states are tidally disrupted, and what composition a distant observer might be able to infer as the signature of such events.

³ Except for the specific case of a helium white dwarf with a hydrogen envelope (Law-Smith et al. 2017a).

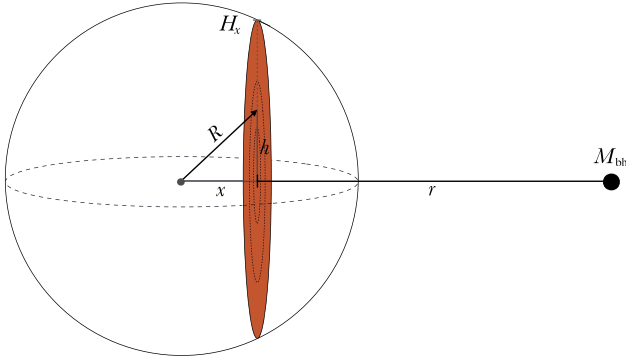


Figure 1. Geometry of the disrupted star and how it can be used to calculate dM/dE . The orange slice represents an equal orbital binding energy surface, which can be approximated as an equal fallback time surface. Here x is the distance from the center of the star along the star’s orbital plane and H_x is the maximum radius of the particular slice. When calculating the equal arrival time surfaces, it is common to neglect any azimuthal or polar deviations. These can be safely neglected given that $(R_*/r_t) = q^{1/3} \ll 1$.

In Section 2, we briefly review the calculation of the mass accretion rate, \dot{M} , onto the SMBH, originally derived by Lodato et al. (2009), and propose a simple generalization that allows \dot{M} to be estimated from realistic stars. In Section 3, using this new framework, we present the accretion rate for stars ranging in mass from 0.8 to $3.0 M_\odot$ and in evolutionary state from ZAMS to TAMS. In Section 4, we summarize our findings and discuss how our models can help inform the emission models of TDEs by providing detailed predictions of the abundance of the radiating material.

2. Methods

2.1. The Mass Accretion Rate

If a star with mass M_* and radius R_* is on a parabolic orbit around an SMBH of mass M_{bh} with pericenter distance, r_p , less than the tidal radius, $r_t = R_*(M_{\text{bh}}/M_*)^{1/3} = R_*q^{-1/3}$, the star will be tidally disrupted. Here $q \equiv M_*/M_{\text{bh}}$ is the mass ratio.

When a star is disrupted, the debris moves on approximately ballistic trajectories, with a spread in specific orbital energy that is roughly frozen at r_t . This spread arises because at the time of disruption, the leading portions of the star are deeper in the potential of the SMBH than the trailing portions, which are farther away. The spread in specific energy of the debris, E_t , can be approximated by taking the Taylor expansion of the SMBH’s potential at the star’s location:

$$E_t = GM_{\text{bh}}R_*/r_t^2 = q^{-1/3}E_*, \quad (1)$$

where $E_* = GM_*/R_*$ is the specific self-binding energy of the star. Because most stars that are tidally disrupted in galactic nuclei approach the SMBH on nearly zero energy orbits, E_t determines the fallback timescale for the most tightly bound debris

$$\begin{aligned} t_t &= \frac{\pi}{M_*} \left(\frac{M_{\text{bh}} R_*^3}{2G} \right)^{1/2} \\ &= 0.1 \text{ year} \left(\frac{M_{\text{bh}}}{10^6 M_\odot} \right)^{1/2} \left(\frac{M_*}{M_\odot} \right)^{-1} \left(\frac{R_*}{R_\odot} \right)^{3/2}. \end{aligned} \quad (2)$$

In order to form an accretion flow, the bound stellar debris must lose a significant amount of energy by viscous dissipation

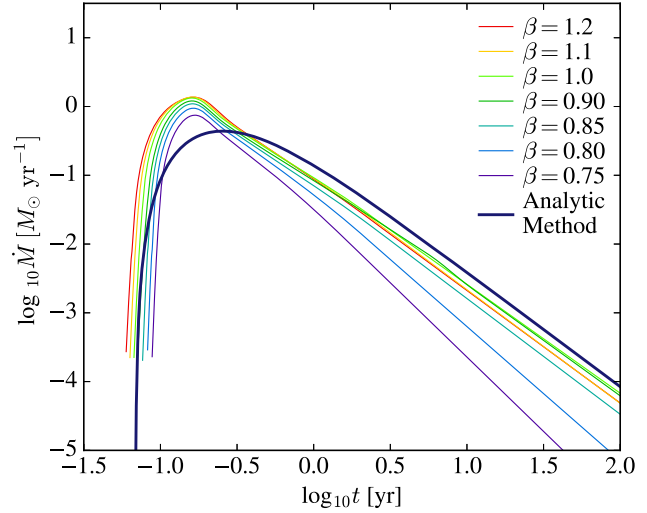


Figure 2. Rate of fallback of stellar debris to pericenter as a function of time from the disruption of a $1 M_\odot$ star calculated using the analytic framework used in this work (thick dark blue line), which assumes a full disruption, compared to those calculated by Guillochon & Ramirez-Ruiz (2013) using hydrodynamical calculations for different β values (thin colored lines). Both calculations use $M_{\text{bh}} = 10^6 M_\odot$ and a star that is constructed as a self-gravitating, spherically symmetric, polytropic fluid with $\gamma = 5/3$.

(Guillochon & Ramirez-Ruiz 2015; Shiokawa et al. 2015; Bonnerot et al. 2016; Hayasaki et al. 2016). If the viscosity is large enough to allow accretion onto the SMBH on a timescale shorter than t_t , the luminosity of the flare is expected to follow the rate of mass fallback $\dot{M} = (dM/dE)(dE/dt) \propto t^{-5/3}$, where $dM/dE = M_*/(2E_t)$ for a star on an initially parabolic orbit and $q \ll 1$ (Rees 1988; Phinney 1989). The $t^{-5/3}$ dependence of TDE light curves relies on the assumption that the specific energy distribution of stellar debris dE/dM is roughly flat with orbital specific energy, which is only valid at late times (Guillochon & Ramirez-Ruiz 2013). At early times, the assumption of constant dM/dE is incorrect and depends sensitively on the structure of the disrupted star (Lodato et al. 2009; Ramirez-Ruiz & Rosswog 2009) and the strength of the tidal interaction (Laguna et al. 1993; Guillochon et al. 2009; Guillochon & Ramirez-Ruiz 2013).

Lodato et al. (2009) and Kesden (2012) moved beyond this simple description by constructing models that explicitly calculate the energy distribution of the disrupted stellar debris to $\mathcal{O}(q^{1/3})$ for stars described by a self-gravitating, spherically symmetric, polytropic fluid. By solving the Lane–Emden equation they determined the density profile of the star, which in turn allowed them to calculate dM/dE . In this paper, we build on their work and show how their formalism can be easily extended to estimate the rate at which the debris falls back to pericenter and is subsequently accreted for tidally disrupted stars with realistic profiles.

The geometrical setup envisioned here is shown in Figure 1. To calculate \dot{M} , we begin by using the standard assumption that the star freezes in at the moment of disruption at r_t . The specific binding energy of a fluid element in this case depends on its position, and dM/dE can be expressed in terms of the star’s initial density profile ρ_* . The mass of a slice of stellar debris dM , defined here as having the same orbital energy, is found by integrating

$$\frac{dM}{dx} = \int_0^{H_x} \rho_*(h) 2\pi h dh, \quad (3)$$

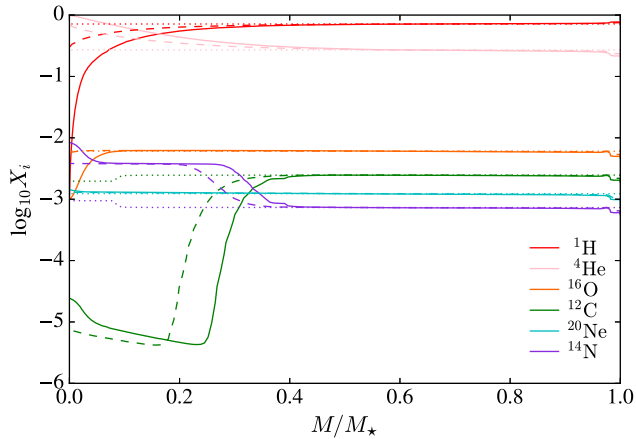


Figure 3. Compositional abundance as a function of enclosed mass in a $1M_{\odot}$ star at three different evolutionary stages during its MS lifetime. In this paper, we characterize evolutionary stages by f_H , the fraction of central hydrogen that has been burned. Here we show the stellar profiles for $f_H = 0.0 = f_{ZAMS}$ (dotted), $f_H = 0.60$ (dashed), and $f_H = 0.99$ (solid), respectively. A $1M_{\odot}$ star disrupted at later stages in its evolution should reveal abundance anomalies: an increase in nitrogen and depletion of oxygen, as previously argued by Kochanek (2016).

where x is measured from the center of the star, H_x is the radius of the slice at a given x , and h is the rescaled height coordinate. If the orbital period t of a given slice is given in terms of its orbital binding energy dE/dx , then the rate dM/dt at which mass falls back to pericenter can be calculated by numerically integrating Equation (3). Using this framework, we calculate the accretion rate history for a large number of realistic stars, whose density profiles we generate using the Modules for Experiments in Stellar Astrophysics (MESA) code. The reader is referred to Section 2.2 for a description of our MESA setup.

The use of this analytic method allows for an extensive study of \dot{M} arising from the disruption of different stars. While this formalism leads to a large reduction in computational expense, it is nonetheless restricted as it relies on the assumption of a spherically symmetric star at the time of disruption. Contrary to what can be predicted by the simple analytical models used in this paper, the rate at which material falls back depends strongly on the strength of the encounter, which can be measured by the penetration factor $\beta \equiv r_i/r_p$.

This is because varying β changes the amount of mass lost by the star, which affects the rate at which the liberated stellar debris returns to pericenter (e.g., Law-Smith et al. 2017a). In Figure 2, we compare fallback curves calculated using the analytical model (thick dark blue line) to those calculated using simulations (thin colored lines). For the purpose of comparison, both models use a $1M_{\odot}$ star with adiabatic index $\gamma = 5/3$ and a $10^6 M_{\odot}$ SMBH. We find that the broad features of \dot{M} are reasonably well captured by the simple model (the same holds true for stars constructed with $\gamma = 4/3$), as was also argued by Lodato et al. (2009) and Kesden (2012). This fact is extremely powerful in that it permits a reasonable characterization of TDE signatures without the need to run many computationally expensive simulations on the large set of stars we study here.

Furthermore, for a fixed β , the time evolution of the forces applied is identical, regardless of the ratio of the star’s mass to the mass of the SMBH. This is because the ratio of the time the star takes to cross pericenter to the star’s own dynamical time depends only on β . Therefore, as long as $q \ll 1$, the tidal

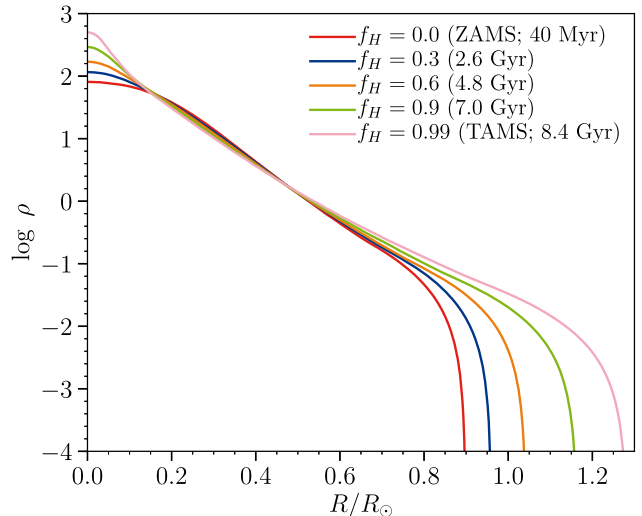


Figure 4. Density profiles for a $1M_{\odot}$ star at different times along its MS evolution. The red line corresponds to ZAMS with a central density of 81 g cm^{-3} and the pink line corresponds to a central hydrogen fraction of 10^{-3} with a central density of 500 g cm^{-3} . These different density profiles result in different r_i and thus exhibit different vulnerability to disruption.

disruption problem is self-similar, and our results can be scaled to predict how the time (Equation (2)) of peak accretion rate, t_{peak} , and its corresponding magnitude \dot{M}_{peak} change with M_{bh} , M_{\star} , and R_{\star} :

$$\dot{M}_{\text{peak}} \propto M_{\text{bh}}^{-1/2} M_{\star}^2 R_{\star}^{-3/2}, \quad (4)$$

and

$$t_{\text{peak}} \propto M_{\text{bh}}^{1/2} M_{\star}^{-1} R_{\star}^{3/2}. \quad (5)$$

This fact is extremely powerful in that it permits us to completely characterize the properties of a disruption of a given star with one calculation. An exception to these simple scalings is if the star penetrates deeply enough such that r_p is comparable to the Schwarzschild radius r_g . In this case, general relativistic effects can alter the outcome, especially if the black hole is spinning (Laguna et al. 1993; Kesden 2012).

We remind the reader that the exact value of the time of peak accretion rate t_{peak} and its corresponding magnitude \dot{M}_{peak} are not precisely determined. Most of these differences arise from how the problem was originally formulated, in which the star’s self-gravity is ignored, and only the spread in binding energy across the star at pericenter is assumed to be important for determining \dot{M} . Our primary goal in this paper is to develop a robust formalism for calculating the rate of fallback and its associated chemical composition as well as conducting a preliminary survey of the key stellar evolution parameters associated with this problem. The formalism presented in this section is well suited to this goal.

2.2. Stellar Models

We use the open source MESA code (Paxton et al. 2011) to calculate the structure and composition of the stars that will be disrupted. We generated 192 solar metallicity stellar profiles ranging in mass from 0.8 to $3.0 M_{\odot}$ and evolutionary state from the zero-age main sequence (ZAMS) to the near terminal-age main sequence (TAMS). Profiles are spaced in intervals of 0.05 in central hydrogen fraction.

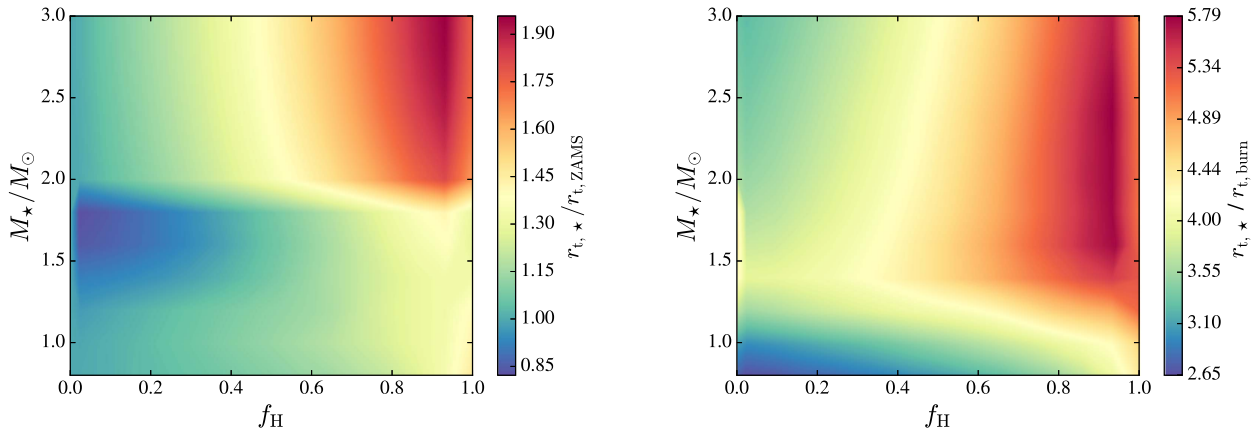


Figure 5. In both panels, the color scale shows the tidal radius of the disrupted star. Left panel: plotted are the ratio of the star’s tidal radius to the tidal radius of that same star at ZAMS ($f_{\text{H}} = 0.0 = f_{\text{ZAMS}}$). This shows that the star’s vulnerability to disruption increases with age. This effect is stronger for more massive stars. Right panel: plotted are the ratio of the tidal radius to $r_{\text{t,burn}}$. Here $r_{\text{t,burn}}$ is defined as the tidal radius of the star’s core undergoing active nuclear burning, where the specific power from nuclear reactions is greater than $1 \text{ erg g}^{-1} \text{ s}^{-1}$. This shows that all of the stars in our study require deeper encounters to strip mass from their burning regions.

The MESA setup used here is described below.⁴ We begin with a pre-MS model, use the `mesa_49` nuclear network with the `jina` rates preference, the Asplund et al. (2009) abundances ($X = 0.7154$, $Y = 0.2703$, and $Z = 0.0142$), and `mixinglengthalpha = 2.0`. The final profile, which we call TAMS, is at a central hydrogen fraction of 10^{-3} . Time steps are limited to a maximum change in central hydrogen fraction of 1%.

We consider the mass range of $0.8\text{--}3.0 M_{\odot}$ as stars with masses below $0.8 M_{\odot}$ will not evolve appreciably over the age of the universe, and stars with masses above $3 M_{\odot}$, with MS lifetimes < 300 Myr, are unlikely to be disrupted (the relaxation time for most galactic nuclei is $\gg 300$ Myr).

We do not consider evolved stars for two reasons. First, the contribution of evolved stars to the current and near-future tidal disruption population is expected to be modest (MacLeod et al. 2012). Second, studies of the tidal disruption of evolved stars such as MacLeod et al. (2012) have shown that even for large β , giant stars are effective at retaining envelope mass and effectively retaining their cores (where the differences in composition arise from MS and post-MS evolution). In this paper, we are interested in the evolved material in the innermost layers of stars that can be reasonably revealed during a TDE and thus we do not focus on significantly evolved stars.

2.3. Salient Model Features

Here we briefly discuss the stellar evolution features that are central to our study; these arise from changes in mass and evolutionary state along the MS. The two main burning processes in MS stars, the p-p chain and the CNO cycle, are highly sensitive to interior temperatures (Kippenhahn et al. 2012) and contribute differently to stars of varying mass. The p-p chain, which increases the abundance of ${}^4\text{He}$ in stars, roughly dominates for masses $\lesssim 1.5 M_{\odot}$. For masses $\gtrsim 1.5 M_{\odot}$ the CNO cycle dominates. During the CNO cycle, fusing hydrogen to helium results in an increase (decrease) of ${}^{14}\text{N}$ (${}^{16}\text{O}$) abundance, with ${}^{12}\text{C}$ acting as a catalyst for the entire cycle. As argued by Kochanek (2016), strong compositional

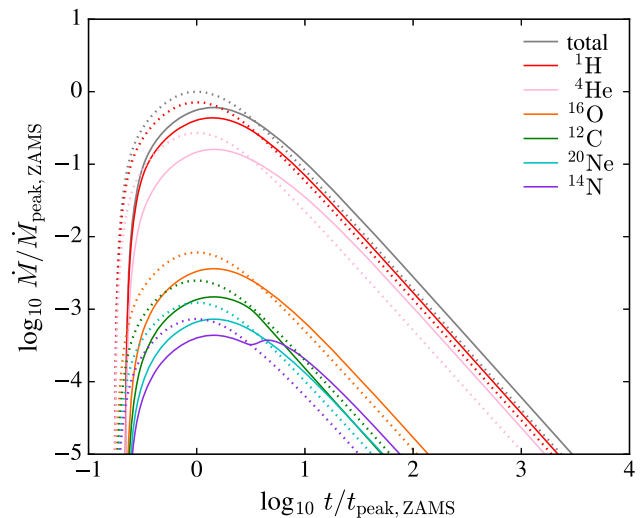


Figure 6. Mass fallback rates for elements that make up 99.6% of the mass of a $1 M_{\odot}$ tidally disrupted star at two different evolutionary stages. The star aged nearly 5 Gyr from the dotted lines ($f_{\text{H}} = 0.0 = f_{\text{ZAMS}}$) to the solid lines ($f_{\text{H}} = 0.60$). \dot{M} for the total mass of the star is shown by the gray curves. All curves are normalized to \dot{M}_{peak} and t_{peak} for the corresponding ZAMS star. The main changes in fallback rates as the star evolves along the MS are an increase in nitrogen and a decrease in carbon after t_{peak} due to CNO activity in the core.

variations are expected in the fallback material of MS stars. In this paper, we trace the abundance variations of the following elements: ${}^1\text{H}$, ${}^4\text{He}$, ${}^{16}\text{O}$, ${}^{12}\text{C}$, ${}^{20}\text{Ne}$, and ${}^{14}\text{N}$. These elements make up at least 99.6% of each star’s total mass. The ${}^{34}\text{S}$ contribution and abundance ratio is very similar to that of ${}^{20}\text{Ne}$ and is thus not explicitly shown in this paper. In what follows, we present abundances relative to solar.

As an example, in Figure 3, we show the compositional variations along the MS for a $1 M_{\odot}$ star with solar abundance at ZAMS. The differently styled lines correspond to different stellar ages as defined by f_{H} , the fraction of central hydrogen burned. A star will have $f_{\text{H}} = 0$ at ZAMS and $f_{\text{H}} = 0.99$ near the end of its MS lifetime. At ZAMS, the star has solar composition (dotted lines) and is roughly homogeneous. After 4.8 Gyr (dashed lines), when more than half of the central hydrogen has been processed ($f_{\text{H}} = 0.60$), the following

⁴ Inlists are available upon request.

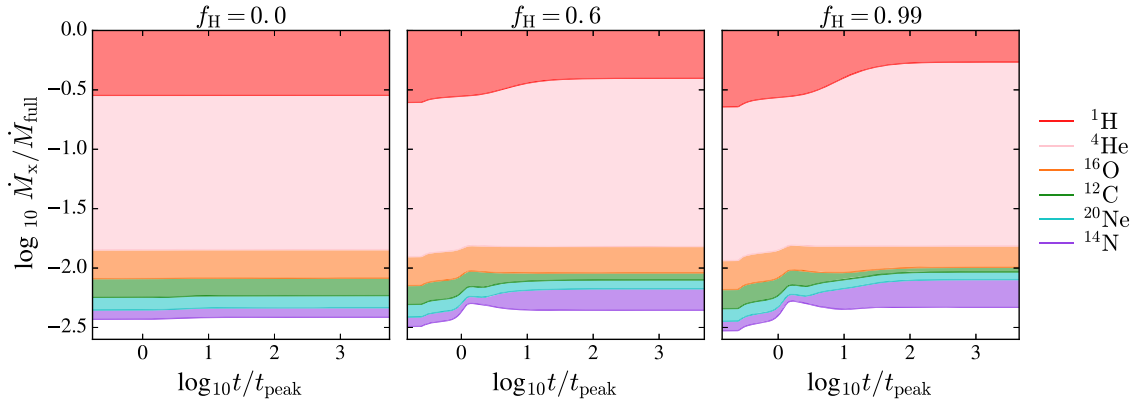


Figure 7. Fallback rate for different elements, \dot{M}_x , following the disruption of a $1 M_\odot$ star at three different evolutionary stages. The left and center panels correspond to the dotted and solid lines shown in Figure 6, respectively. The right panel shows \dot{M} for the same star but at $f_H = 0.99$, which corresponds to an age of 8.3 Gyr. Time is in units of t_{peak} . As the star ages, we see an increase in nitrogen and a decrease in carbon abundance but only after t_{peak} .

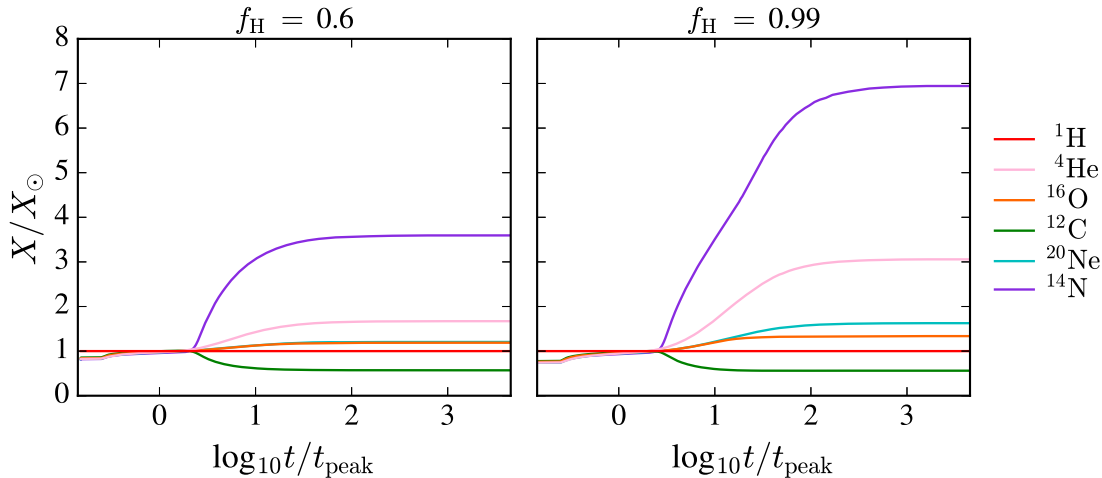


Figure 8. Elemental abundance of the fallback material relative to solar following the disruption of a $1 M_\odot$ at two different evolutionary stages: $f_H = 0.60$ (left panel) and TAMS (right panel). A rapid evolution of ^{14}N and ^{12}C abundance relative to the other elements is clearly seen. The solar ratios clearly illustrate the significance of the variations in the abundances of ^{16}O , ^4He , and ^{20}Ne .

abundance variations are seen: a significant increase of ^{14}N , a modest increase (decrease) of ^4He (^1H), a significant decrease of ^{12}C , and a roughly unchanged abundance of ^{20}Ne and ^{16}O . At TAMS (solid lines), where most of the central hydrogen has been processed ($f_H = 0.99$), a depletion in ^{16}O abundance is also observed. At this late stage, there is also a secondary increase in ^{14}N in the core of the star.

In summary, we see that ^1H , ^4He , and ^{16}O abundances evolve gradually, slowly extending to larger parts of the star and encompassing larger radii, while ^{12}C and ^{14}N abundances evolve rapidly across the burning region. All stars follow a similar trend. The most massive star in this study ($3 M_\odot$) has, at TAMS, large compositional changes across roughly half of its mass (or about 20% of its radius). As discussed by Kochanek (2016), in the fallback material from a TDE, we expect ^{12}C and ^{14}N abundance anomalies to be more noticeable and appear at earlier times than the other elemental anomalies.

As a star evolves along the MS, its average density, $\bar{\rho}_*$, decreases and its core density, ρ_{core} , increases. This is illustrated in Figure 4, where we show the evolution of the density profile for a $1 M_\odot$ star with initial solar abundance from ZAMS to TAMS. Since the star’s radius increases with age, while its mass remains nearly constant, $\bar{\rho}_*$ decreases with age.

The effects of $\bar{\rho}_*$ on the star’s vulnerability to tidal deformations can be readily seen by rewriting r_t as $r_t \simeq M_{\text{bh}}^{1/3} \bar{\rho}_*^{-1/3}$. This scaling implies that as the star evolves, it becomes progressively more vulnerable to tidal deformations and mass loss. However, this scaling is unable to accurately capture the exact impact parameter required to fully disrupt a star. This is because as the star evolves a denser core, a surviving core is likely to persist for a disruption at r_t ($\beta = 1$), which is the penetration factor assumed for the analytical calculations. Nonetheless, we expect the time and magnitude of the peak accretion rate to be reasonably well captured by the simple formalism described here.

3. The Disruption of Evolved MS Stars

3.1. Tidal Vulnerability

Here we analyze how the tidal radius, $r_{t,*}$, evolves with stellar mass and age along the MS for the stars in our study. The left panel of Figure 5 shows $r_{t,*}$ normalized to the tidal radius of the same star at ZAMS, $r_{t,\text{ZAMS}}$. We plot this ratio as a function of f_H , the fraction of central hydrogen burned, and stellar mass M_* . As expected, we find that the tidal radius increases with age and evolves more dramatically with f_H

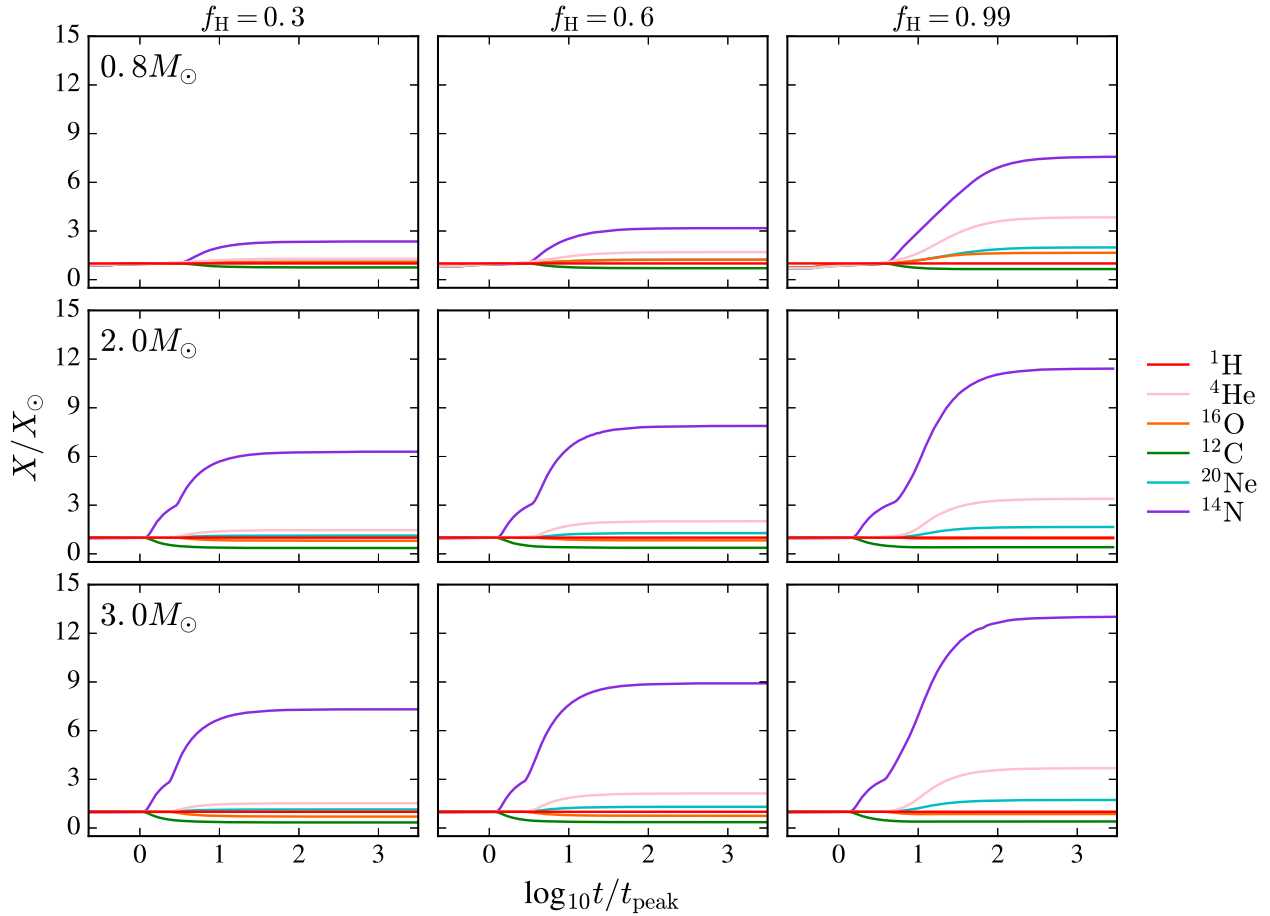


Figure 9. Relative abundance of stellar debris as a function of fallback time arising from the disruption of $0.8 M_{\odot}$ (top row), $2.0 M_{\odot}$ (middle row), and $3.0 M_{\odot}$ (bottom row) stars at three different evolutionary stages ($f_{\text{H}} = 0.3, 0.6,$ and 0.99). The change in abundance relative to solar is observed to increase with mass and age but only after t_{peak} . These anomalies appear at earlier times for higher mass stars.

throughout the lifetime of more massive stars. For example, the tidal radius of a $3 M_{\odot}$ star increases by roughly a factor of two over its MS lifetime. As stars move along the MS, they become progressively more vulnerable to tidal dissipation and mass stripping.

Next, we discuss how the vulnerability of regions with processed element abundances compares to that of the entire star. The right panel of Figure 5 shows the ratio of $r_{t,*}$ to $r_{t,\text{burn}}$, where $r_{t,\text{burn}}$ is defined as the tidal radius of material within the regions of a star that exhibit active nuclear burning. This region of active nuclear burning is defined to be where the specific power from nuclear reactions is greater than $1 \text{ erg g}^{-1} \text{ s}^{-1}$. This is a consistent way of defining the burning region throughout all of the stellar profiles calculated here. As expected, this region is located at small radii where the density is much higher than $\bar{\rho}_{*}^{-1/3}$ and thus deeper penetrations are required in order to observe the evolved element abundances in the fallback material. Also, as this region is located within the innermost layers of the star, the processed elements will be revealed in the fallback material only at later times.

3.2. The Disruption of a Sun-like Star

Figure 6 shows the mass fallback rate arising from the full disruption of a $1 M_{\odot}$ star at two different evolutionary states: at ZAMS (dotted lines) and after 4.8 Gyr (dashed lines), when

more than half of the central hydrogen has been processed ($f_{\text{H}} = 0.60$). These curves are normalized to the peak fallback rate and peak time of the corresponding ZAMS star: $\dot{M}_{\text{peak,ZAMS}}$ and $t_{\text{peak,ZAMS}}$, respectively. The compositions of the stars before disruption are shown in Figure 3 as dotted (ZAMS) and dashed ($f_{\text{H}} = 0.60$) lines. The disruption of the TAMS $1 M_{\odot}$ star, whose composition is shown by the solid lines in Figure 3, is expected to be similar in shape to the disruption of the $f_{\text{H}} = 0.60$ star, with an enhancement in ^{14}N and depletion in ^{12}C .

The smooth behavior of the fallback rates for all the plotted elements during the disruption of the ZAMS star (dotted lines in Figure 3) is the result of the nearly homogeneous elemental composition within the star. The fallback rates for the $f_{\text{H}} = 0.60$ star (dashed lines in Figure 3), on the other hand, contain information about the varying nature of its elemental composition. In the fallback rates, we can see an obvious increase in ^{14}N , a decrease in ^{12}C , and a slight increase in ^4He , which is consistent with the compositional structure of the star before disruption. These results are in agreement with Kochanek (2016). We note that the fallback curves for the $f_{\text{H}} = 0.60$ star have no abundance variations at $t \lesssim t_{\text{peak}}$. These compositional anomalies might provide insight into the nature of the progenitor star near or after the most luminous time of the tidal disruption flare.

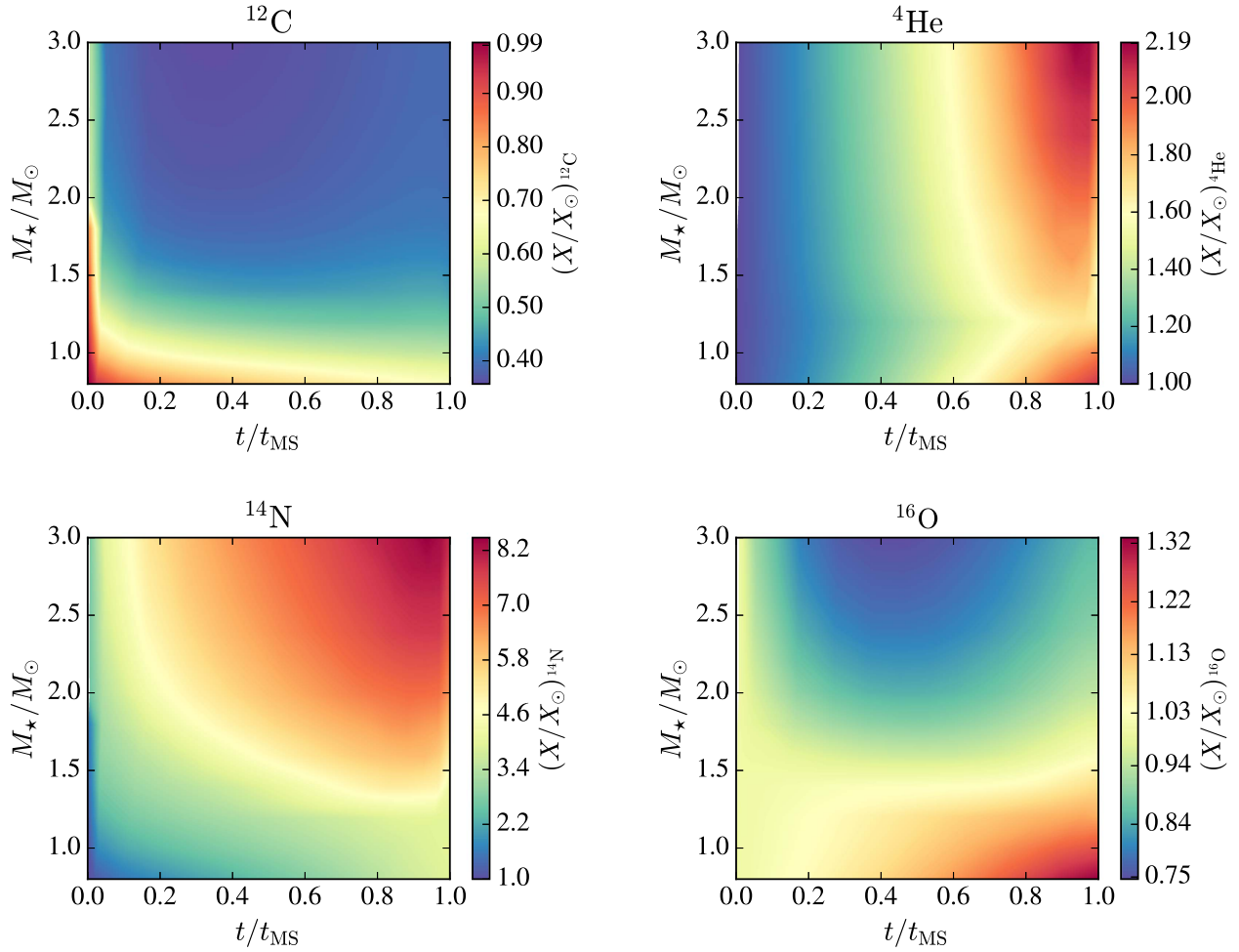


Figure 10. Elemental abundances relative to solar at the time the mass fallback rate has reached one-tenth of its peak value, $t_{0.1} > t_{\text{peak}}$, for all of the stellar masses and ages in our sample. Elements of interest are ^{12}C , ^4He , ^{14}N , and ^{16}O . Values are shown as a function of the star’s fractional main-sequence lifetime and stellar mass. We find carbon abundances to be more indicative of stellar mass for $M_* \lesssim 1.5 M_\odot$, while helium abundances are correlated with stellar age for all masses. $(X/X_\odot)^{14\text{N}} \gtrsim 5.0$ occurs only for masses greater than $1.5 M_\odot$ and develops early in the star’s evolution. We also find oxygen abundances to be primarily stellar mass dependent.

In Figure 7, we show the fractional contribution to the total fallback rate arising from each element during the disruption of a $1 M_\odot$ star at three different evolutionary stages. From left to right, these panels correspond to the ZAMS (dotted), $f_{\text{H}} = 0.60$ (dashed), and TAMS (solid) composition profiles in Figure 3, respectively. In each panel, we calculate the ratio of the fallback rate for each element, \dot{M}_X , to the total mass fallback rate, \dot{M}_{full} .

For the disruption of a $1 M_\odot$ star, it might be challenging to distinguish its evolutionary stage using spectral information if it is only obtained at $t \lesssim t_{\text{peak}}$ (though the exact values of \dot{M}_{peak} and t_{peak} are expected to be distinct; Figure 12). This is, however, not the case after t_{peak} .

Figure 8 shows the abundance of the fallback material relative to solar following the disruption of a $1 M_\odot$ at two different evolutionary stages: $f_{\text{H}} = 0.60$ (left panel) and TAMS (right panel). Elemental abundances relative to solar are calculated here using

$$\frac{X}{X_\odot} = \frac{\dot{M}_X / \dot{M}_{\text{H}}}{M_X / M_{\text{H}, \odot}}, \quad (6)$$

where \dot{M}_X is the fallback rate for a selected element, \dot{M}_{H} is the fallback rate of ^1H , and $M_X / M_{\text{H}, \odot}$ is the abundance mass ratio relative to solar of element X. The disruptions of a $f_{\text{H}} = 0.60$ and a TAMS star each show a significant increase in ^{14}N and ^4He after t_{peak} . As expected, these features are more prominent for the TAMS star. Near $t = 10t_{\text{peak}}$, Figure 8 shows steeper abundance gradients in the right panel compared to the left in all elements except ^{12}C . We note that these values are relative to ^1H . This is important in the case of ^{16}O and ^{20}Ne , where we see an increase in their abundance. This is because while ^1H is depleted at every evolutionary stage, ^{16}O and ^{20}Ne abundances remain relatively constant for a star of this mass, which results in higher solar ratios. However, this behavior is also altered by the mass of the star as we discuss in the following section.

3.3. Disruption of MS stars

For reasons discussed previously, it seems likely that the evolutionary state of a star might be revealed by charting the compositional evolution of the fallback material, which might be inferred from particular features in the spectra of the resulting luminous flare. The association of a significant

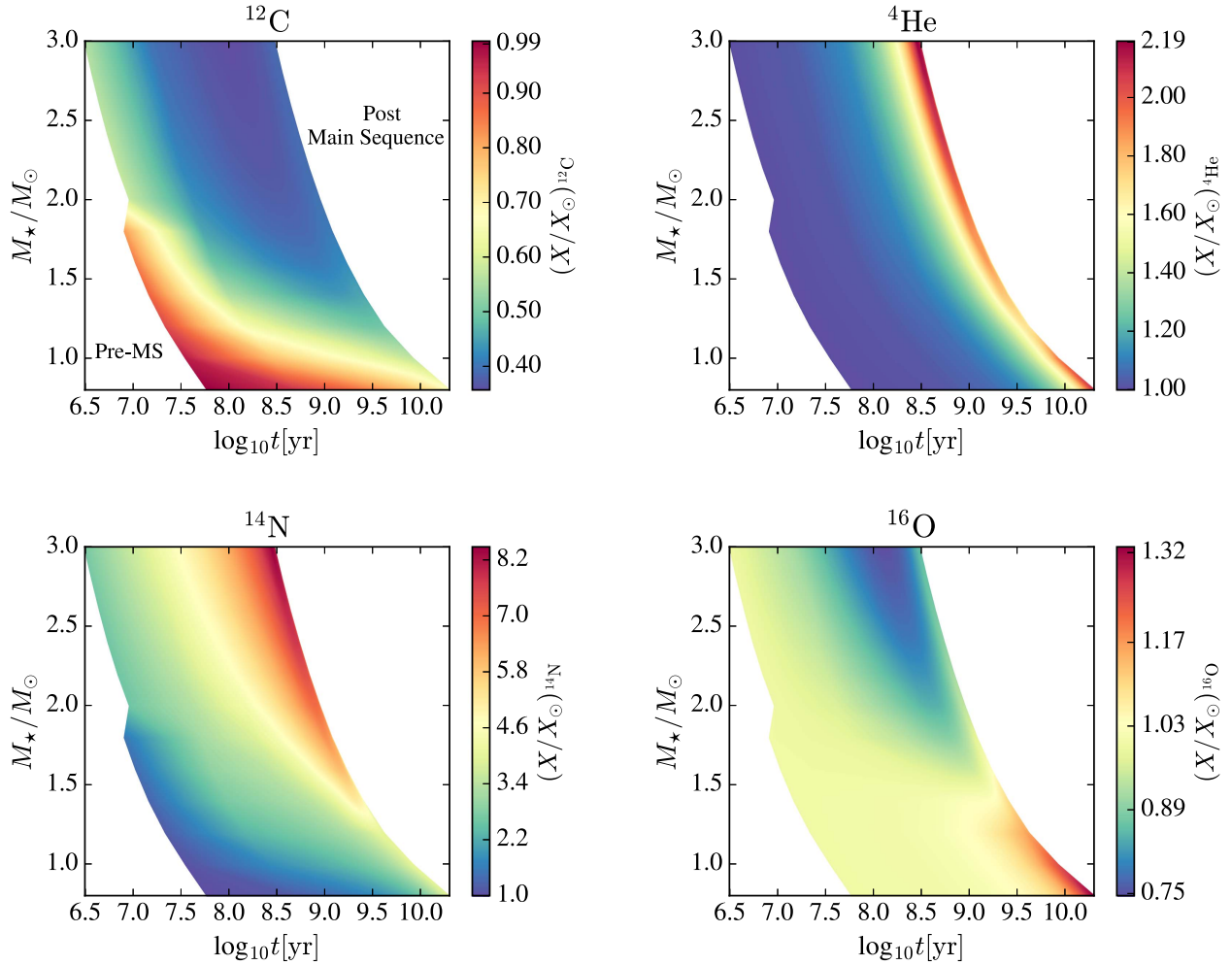


Figure 11. Same as Figure 10 but presented with stellar age in years (x-axis). The white regions correspond to pre-MS (left) or post-MS (right).

fraction of TDEs with post-starburst galaxies (Arcavi et al. 2014; French et al. 2016, 2017; Law-Smith et al. 2017b) has suggested the likely presence of evolved stars in the nuclei of TDE hosts, or at least a subset thereof. Much of our effort in this section will thus be dedicated to determining the state of the fallback material after the tidal disruption of stars of a wide range of ages and masses.

In Figure 9, we show the relative abundances of the fallback material for three representative MS star disruptions. The first row of panels shows the abundance of the fallback material for a $0.8 M_{\odot}$ star tidally disrupted at three different evolutionary stages: $f_{\text{H}} = 0.3$, $f_{\text{H}} = 0.6$, and $f_{\text{H}} = 0.99$. The abundances shown are similar to those shown in Figure 8 for a $1 M_{\odot}$ star. At these low masses, we expect the abundance anomalies to be present in the fallback material at a few times t_{peak} .

The second row of panels in Figure 9 shows the relative abundances of the fallback material for a disrupted $2 M_{\odot}$ star. The abundance patterns are broadly similar to those seen for the $0.8 M_{\odot}$ and $1 M_{\odot}$ stellar disruptions. However, there are three main differences. First, in contrast to the observed increase of ^{16}O seen in the $0.8 M_{\odot}$ and $1.0 M_{\odot}$ disruptions, a significant decrease in ^{16}O abundance is observed. This is an indication of the increased CNO activity in the $2 M_{\odot}$ star. Second, two distinct bumps are seen in the evolution of the ^{14}N abundance, contrary to its steady increase in the smaller mass disruptions.

The first increase in the ^{14}N abundance (and the corresponding ^{12}C depletion) is due to the local maximum of CNO burning that is located at roughly 20% of the star’s radius. There is also significant CNO and p–p chain activity in the star’s core, which is revealed at later times in the fallback material, and leads to the relatively delayed increase in ^4He and ^{20}Ne , the corresponding decrease of ^{16}O , and a secondary increase in ^{14}N . Third, abundance variations are observed significantly closer to t_{peak} in the $2 M_{\odot}$ disruptions than in the $0.8 M_{\odot}$ disruptions. This is a result of the more extended burning region within the star, whose material is revealed at earlier times following the disruption.

In the bottom row of panels in Figure 9, we show the composition of the fallback material following the disruption of a $3 M_{\odot}$ star. The abundance variations in these fallback curves closely resemble those for the $2 M_{\odot}$ star, but with larger variations appearing at earlier times. The abundance variations presented in Figure 9 for the few representative stars accurately describe the overall trends in our sample. These trends are illustrated in Figure 10, in which various elemental abundances are shown at the time that the mass fallback rate has reached one-tenth of its peak value, $t_{0.1} > t_{\text{peak}}$.

The fallback abundances at $t_{0.1}$ are plotted in Figure 10 as a function of the star’s fractional main-sequence lifetime, t/t_{MS} , and stellar mass. In Figure 11, we show the same abundance

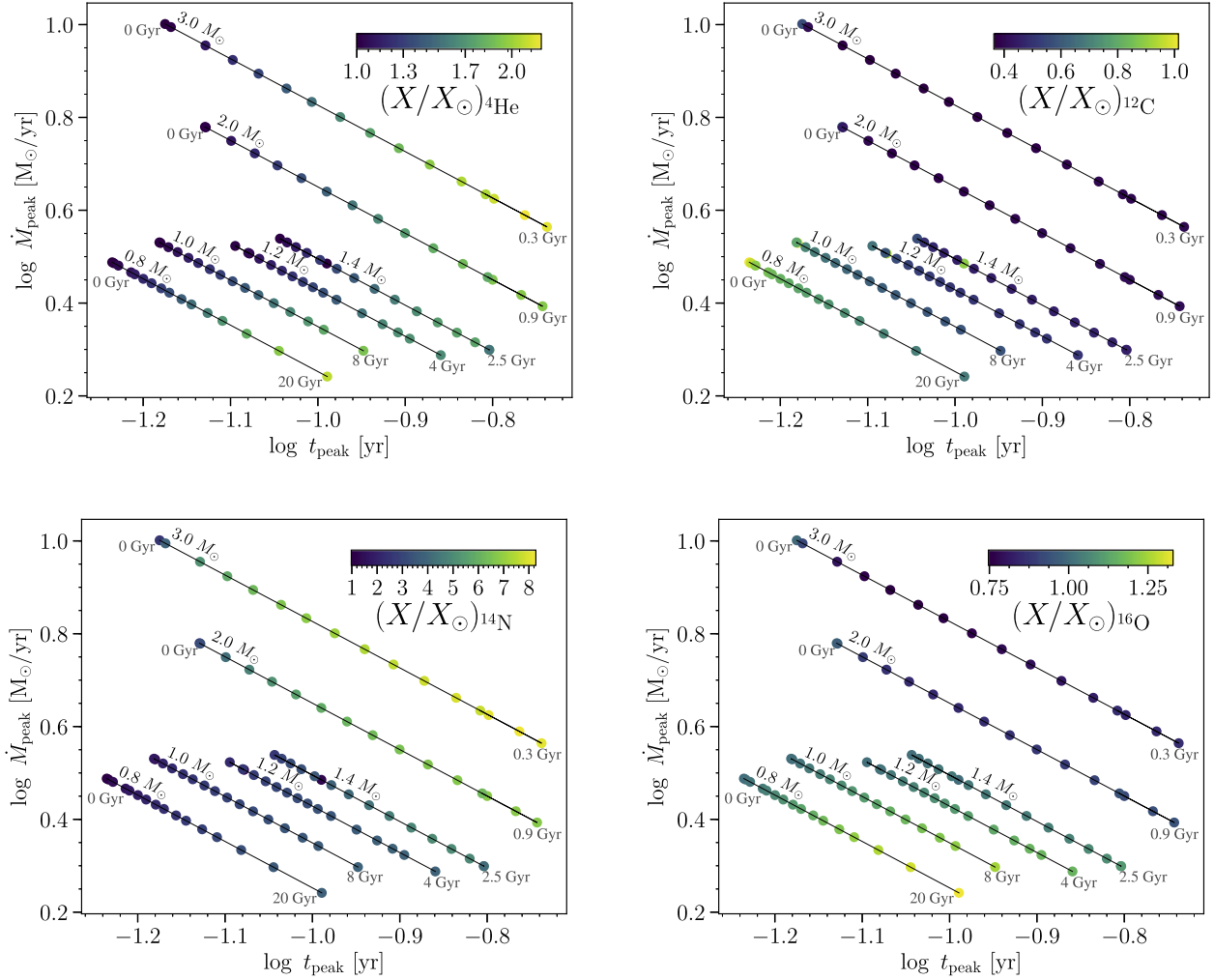


Figure 12. Fallback abundance at $t_{0.1}$ of ${}^4\text{He}$, ${}^{12}\text{C}$, ${}^{14}\text{N}$, and ${}^{16}\text{O}$ (clockwise from top left) for the disruption (by a $M_{\text{bh}} = 10^6 M_{\odot}$ SMBH) of $0.8 M_{\odot}$, $1 M_{\odot}$, $1.2 M_{\odot}$, $1.4 M_{\odot}$, $2.0 M_{\odot}$, and $3.0 M_{\odot}$ stars along their MS evolution. Abundances are at $t_{0.1}$, but points are placed at \dot{M}_{peak} and t_{peak} for the disruption of each star. Abundances are quoted relative to solar. Points are roughly equally spaced in time for each mass, with the top-left-most point being ZAMS and the bottom-right-most point being TAMS. (This is not strictly true for the ZAMS point of the $1 M_{\odot}$, $1.2 M_{\odot}$, and $1.4 M_{\odot}$ stars as their radius slightly decreases at the very beginning of their MESA evolution, but all other points for these stars proceed left to right with age as the star subsequently evolves.)

values as in Figure 10 but presented with the evolutionary age of the star in years. Some key points should be emphasized. We find carbon decrements to be indicative of stellar mass, while helium enhancements are indicative of age. $(X/X_{\odot})^{14\text{N}} \gtrsim 5.0$ occurs only for masses greater than $1.5 M_{\odot}$ and develops early in the star’s evolution. This is due to the enhanced CNO activity inside the more massive stars in our sample. We also find oxygen abundances to be primarily dependent on stellar mass.

The processes discussed here suggest that TDEs may have a more complex spectrum and time-structure than simple models suggest. The effects are especially interesting when the accretion rate is high, as this gives rise to high luminosities, and thus can more readily offer clues to the nature of the disrupted star. The specific values of \dot{M}_{peak} and t_{peak} can further aid in distinguishing the properties of the progenitor star before disruption. This is illustrated in Figure 12 where we show abundances of carbon, helium, nitrogen, and oxygen (relative to solar) in the fallback debris as a function of \dot{M}_{peak} and t_{peak} . Each panel in Figure 12 corresponds to a different element, the different lines correspond to different stars in our study ($0.8 M_{\odot}$, $1.0 M_{\odot}$, $1.2 M_{\odot}$, $1.4 M_{\odot}$,

$2.0 M_{\odot}$, and $3.0 M_{\odot}$), the points are different stages in the stars’ evolution on the MS (roughly equally spaced in time), and the color of the points is the abundance of the fallback debris at the time that \dot{M} falls to one-tenth of its peak value, $t_{0.1}$. We used the fitting formulas presented in Guillochon & Ramirez-Ruiz (2013), which give \dot{M}_{peak} and t_{peak} given β , γ , M_{\star} , and R_{\star} . We used $\gamma = 4/3$ and its corresponding penetration factor for full disruption ($\beta = 1.85$) given by Guillochon & Ramirez-Ruiz (2013). The values of M_{\star} and R_{\star} were taken from the MESA profiles and we have assumed $M_{\text{bh}} = 10^6 M_{\odot}$ (the reader is referred to Equations (4) and (5) for the scalings of \dot{M}_{peak} and t_{peak} with M_{bh} , respectively). The abundance values are the same as in Figure 10.

The variation in elemental abundances is accompanied by a wide range in \dot{M}_{peak} and a moderate range in t_{peak} ; a combination of these different pieces of information can help characterize the progenitor stars of TDEs. For example, the disruption of a $3 M_{\odot}$ star has similar t_{peak} values to that of a $2 M_{\odot}$ star. While their ${}^{12}\text{C}$ and ${}^{16}\text{O}$ abundances are very similar, the $3 M_{\odot}$ star’s disruption results in a higher abundance in ${}^{14}\text{N}$ and ${}^4\text{He}$ at every stage in its

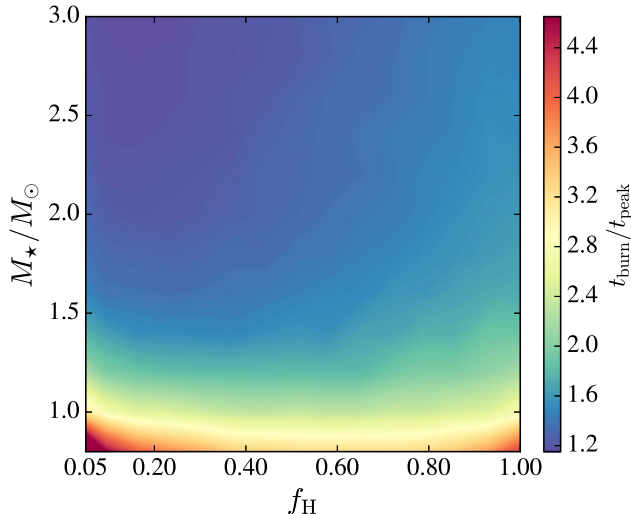


Figure 13. Ratio of t_{burn} to t_{peak} as a function of f_{H} and stellar mass. Here t_{burn} is the time when non-solar abundance ratios begin to appear in the fallback material, specifically when the abundance of ^{12}C and ^{14}N deviate from solar. We have explicitly excluded $f_{\text{H}} \lesssim 0.05$ from this plot, given that these stars experience some mild contraction early in their MESA evolution. The ratio ($t_{\text{burn}}/t_{\text{peak}}$) reaches a maximum (minimum) value of 7.6 (1.15) for a $0.8 M_{\odot}$ ($3 M_{\odot}$) star at $f_{\text{H}} = 0.05$ ($f_{\text{H}} = 0.23$).

evolution, along with a higher \dot{M}_{peak} . In the lower mass stars ($0.8\text{--}1.4 M_{\odot}$) there are many degeneracies in \dot{M}_{peak} and t_{peak} values. Here, the ^{14}N , ^{16}O , and ^4He abundances are similar (over the age of the universe) but the ^{12}C abundances vary at the early stages in these stars’ MS evolution. Compositional information, combined with reprocessing and radiative transfer calculations (e.g., Roth et al. 2016), can thus be used to discern the stellar mass and age of the disrupted star.

4. Discussion

4.1. Summary of Key Results

Motivated by the work of Kochanek (2016), we have modeled the tidal disruption of MS stars of varying mass and age. We adopted the analytic formalism originally presented in Lodato et al. (2009) to study, for the first time, the time evolution of the composition of the fallback debris onto the SMBH. We compared the analytic method to hydrodynamic simulations in Figure 2 and found, similarly to Lodato et al. (2009) and Kesden (2012), that the broad features of the fallback curves are reasonably well captured by it.⁵ We quantify the variations in composition arising from the disruption of 12 different stars with masses of $0.8\text{--}3.0 M_{\odot}$ at 16 different evolutionary stages along the MS. The main results of our study are the following.

- 1 We predict an increase in nitrogen and depletion in carbon abundance in the fallback debris with MS evolution for all stars in our sample (in agreement with Kochanek 2016). We find a decrease in oxygen with MS evolution for $M_{\star} \gtrsim 1.5 M_{\odot}$, and an increase for $M_{\star} < 1.5 M_{\odot}$.
- 2 For all of the TDEs modeled in this study, we find that the time during the fallback rate curve when anomalous

abundance features are present, t_{burn} , is after the time of peak fallback rate t_{peak} .

- 3 Abundance variations are more significant and $t_{\text{burn}}/t_{\text{peak}}$ is smaller for stars of larger mass.
- 4 Some key variations in the compositional evolution are highlighted, along with the types of observations that would help to discriminate between different stellar disruptions. In particular, we find carbon and oxygen abundances to be strongly dependent on stellar mass for $M_{\star} \lesssim 2 M_{\odot}$, while helium abundances are found to be correlated with stellar age for all masses. $(X/X_{\odot})^{14\text{N}} \gtrsim 5.0$ occurs only for masses greater than $1.5 M_{\odot}$ and is observed early in the star’s evolution.
- 5 Studying the compositional variation in the fallback debris provides a clear method for inferring the properties of the progenitor star before disruption.

4.2. Implications for Observations and Models

It is evident from the results described above that the evolution of the interior structure of stars during their MS lifetimes is very rich. Even in the simplest case of a Sun-like star, complex behavior with multiple abundance transitions in the fallback material may be observed. The resulting TDE spectra are expected to depend fairly strongly on the abundance properties of the fallback material (Roth et al. 2016). This implies that if one can be very specific about the times at which we expect to see such transitions in the observed emission, one can better constrain the properties of the disrupted star.

Motivated by this, in Figure 13, we plot the fallback time t_{burn} , relative to t_{peak} , at which we expect to see anomalous abundance variations. Here t_{burn} is defined as the time at which the abundances of ^{12}C and ^{14}N in the fallback material, as presented in Figures 8 and 9, both deviate from unity. $t_{\text{burn}}/t_{\text{peak}}$ is shown in Figure 13 as a function of stellar mass and age (characterized by f_{H}). At fixed f_{H} , we see that non-solar abundances in the fallback debris begin to appear systematically closer to t_{peak} as stellar mass increases. For the $3.0 M_{\odot}$ star, $t_{\text{burn}} \approx 1.2 t_{\text{peak}}$ for $f_{\text{H}} \lesssim 0.3$. For constant M_{\star} , $t_{\text{burn}}/t_{\text{peak}}$ increases mildly with f_{H} for stars with $M_{\star} > 1.6 M_{\odot}$. For stars with $M_{\star} < 1.6 M_{\odot}$, this ratio remains fairly constant throughout the star’s evolution. In summary, t_{burn} depends strongly on M_{\star} but has a relatively weak dependence on stellar age. It is important to note that independently of the mass and age of the disrupted star, no anomalous abundances are expected to be observed before t_{peak} .

Information regarding the nature of the disrupted star should be imprinted on the properties of the TDE light curve (e.g., t_{peak} and \dot{M}_{peak}) and spectrum (particularly at $t \gtrsim t_{\text{burn}}$). Current observations of TDEs show clear differences in their rise and decay properties as well as in their spectral evolution. Peculiar emission features have been observed in their spectra, which include an array of helium, hydrogen, and nitrogen broad line emission features. The origin of these features as well as their associated line ratios have caused significant debate. The extreme helium to hydrogen line ratio observed in the transient event PS1-10jh was initially proposed to be the result of the tidal disruption of a helium-rich star (Gezari et al. 2012). However, such line ratios have also been shown to arise from the reprocessing of radiation through the fallback debris of a disrupted Sun-like star (Roth et al. 2016). As for the additional presence of rare nitrogen features, Kochanek (2016) first

⁵ This work should, however, be taken only as a guide for the expected compositional trends in the fallback material, as hydrodynamical simulations are needed to accurately predict the evolution and characteristics of the flares.

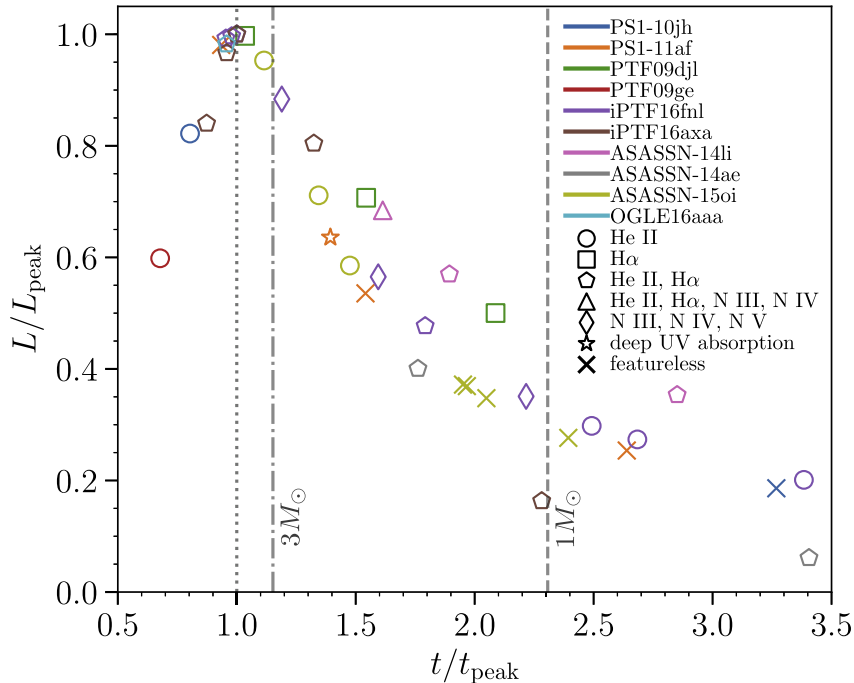


Figure 14. Compositional features in the spectra of well-sampled tidal disruption events with existing spectroscopic observations. The y- and x-axes show luminosity and time relative to peak, respectively, with different colors corresponding to distinct events, and different symbols corresponding to different spectral features. We show the minimum values of $t_{\text{burn}}/t_{\text{peak}}$ (Figure 13) as derived from our study for a $1 M_{\odot}$ (dashed line) and $3 M_{\odot}$ (dashed-dotted line) star.

proposed that the disruption of MS stars with evolved stellar compositions could lead to enhanced nitrogen (as well as anomalous helium and carbon abundances).

In Figure 14, we show compositional features in the spectra of 10 observed TDEs. We place each spectrum in the light curve of each event, relative to its peak luminosity and peak time. Symbols indicate features present in the spectra. Bolometric light-curve fits for each event are from Mockler et al. (2018). Data is taken from Gezari et al. (2012, 2015), Chornock et al. (2014), Arcavi et al. (2014), Brown et al. (2016, 2017, 2018), Blagorodnova et al. (2017), Hung et al. (2017), Holoien et al. (2014, 2016a, 2016b), Cenko et al. (2016), and Wyrzykowski et al. (2017). Note that this figure shows TDEs with well-sampled light curves and existing spectroscopic observations. Several TDE spectra show compositional features at or near the peak in their light curve. Our calculations (in particular, see Section 3.3 and Figure 13) predict no compositional abundance changes (relative to solar) in the fallback material at or near peak due to the star. This implies that the strong suppression of hydrogen Balmer line emission relative to helium line emission should occur even at solar composition, as argued by Roth et al. (2016), due to optical depth effects alone. For observations at $t > t_{\text{burn}}$, we expect the reprocessing material to be enhanced in helium, yet the optical depth effects are expected to be less important (Guillochon et al. 2014). As such, radiation transfer calculations are needed before firm conclusions can be derived from observations of evolving line ratios in a given TDE.

Nitrogen emission lines, on the other hand, are only currently detected at $t \gtrsim 1.2 t_{\text{peak}}$. If their presence is primarily attributed to a drastic increase in nitrogen abundance, then based on the results shown in Figures 12 and 13, one would conclude that $M_{\star} \gtrsim 1.8 M_{\odot}$ for the star whose disruption triggered the ASASSN-14li flaring event and $M_{\star} \gtrsim 3.0 M_{\odot}$ for

the star whose disruption triggered iPTF16fnl. However, early UV spectra that show a lack of nitrogen emission lines at early times are needed to support constraints such as these. In addition, the line ratio variability of, for example, CIII and NIII, can be used to infer the abundance evolution (as these lines have similar ionization potentials). The timescale for chemical enrichment (i.e., t_{burn}) can thus provide a direct observational test of which stars are being disrupted by the central SMBH.

Much progress has been made in understanding how the feeding rate onto an SMBH proceeds after the disruption of a particular star, and in deriving the generic properties of the flares that follow from this. There still remain a number of mysteries, especially concerning the identity of the star, the nature of the energy dissipation mechanism, and the timescales involved. The modeling of the flare itself (i.e., the dissipation mechanism and the radiation processes) is a formidable challenge to theorists and to numerical techniques. It is also a challenge for observers, in their quest to detect fine details in distant, fading sources. The class of models we have presented here predict that the spectral properties of the fading signals will turn out to be even more telling and fascinating than initially anticipated.



Future work will include a more detailed exploration of the parameters governing the abundance of the fallback material, including hydrodynamical calculations (e.g., Law-Smith et al. 2017a) as well as radiative transfer calculations (e.g., Roth et al. 2016) evolved over time for different properties of the reprocessing material. Studies of this sort, in comparison with improved spectral observations of TDEs, will undoubtedly help clarify the physics governing these transient sources.

We thank B. Mockler for insightful conversations, as well as for providing bolometric light-curve fits for the TDEs shown in

Figure 14. We thank N. Roth, J. Guillochon, R. Foley, and D. Kasen for useful discussions. We thank the anonymous referee for helpful suggestions and comments. M.G.-G. and E.R.-R. are grateful for support from the Packard Foundation and from Julie Packard. J.L.-S. and E.R.-R. acknowledge support from the DNRF, NASA ATP grant NNX14AH37G, and NSF grant AST-1615881.

Software: MESA (Paxton et al. 2011), Astropy (Astropy Collaboration et al. 2018), NumPy (van der Walt et al. 2011), and SciPy (Jones et al. 2001).

ORCID iDs

Jamie Law-Smith  <https://orcid.org/0000-0001-8825-4790>
 Enrico Ramirez-Ruiz  <https://orcid.org/0000-0003-2558-3102>

References

- Arcavi, I., Gal-Yam, A., Sullivan, M., et al. 2014, *ApJ*, **793**, 38
 Asplund, M., Grevesse, N., Sauval, A. J., & Scott, P. 2009, *ARA&A*, **47**, 481
 Astropy Collaboration, Price-Whelan, A. M., Sipőcz, B. M., et al. 2018, arXiv:1801.02634
 Auchettl, K., Guillochon, J., & Ramirez-Ruiz, E. 2017, *ApJ*, **838**, 149
 Blagorodnova, N., Gezari, S., Hung, T., et al. 2017, *ApJ*, **844**, 46
 Bonnerot, C., Rossi, E. M., Lodato, G., & Price, D. J. 2016, *MNRAS*, **455**, 2253
 Brown, G. C., Levan, A. J., Stanway, E. R., et al. 2015, *MNRAS*, **452**, 4297
 Brown, J. S., Holoien, T. W.-S., Auchettl, K., et al. 2017, *MNRAS*, **466**, 4904
 Brown, J. S., Kochanek, C. S., Holoien, T. W.-S., et al. 2018, *MNRAS*, **473**, 1130
 Brown, J. S., Shappee, B. J., Holoien, T. W.-S., et al. 2016, *MNRAS*, **462**, 3993
 Cenko, S. B., Cucchiara, A., Roth, N., et al. 2016, *ApJL*, **818**, L32
 Cenko, S. B., Krimm, H. A., Horesh, A., et al. 2012, *ApJ*, **753**, 77
 Chornock, R., Berger, E., Gezari, S., et al. 2014, *ApJ*, **780**, 44
 Evans, C. R., & Kochanek, C. S. 1989, *ApJL*, **346**, L13
 Frank, J., & Rees, M. J. 1976, *MNRAS*, **176**, 633
 French, K. D., Arcavi, I., & Zabludoff, A. 2016, *ApJL*, **818**, L21
 French, K. D., Arcavi, I., & Zabludoff, A. 2017, *ApJ*, **835**, 176
 Gezari, S., Chornock, R., Lawrence, A., et al. 2015, *ApJL*, **815**, L5
 Gezari, S., Chornock, R., Rest, A., et al. 2012, *Natur*, **485**, 217
 Graur, O., French, K. D., Zahid, H. J., et al. 2018, *ApJ*, **853**, 39
 Guillochon, J., Manukian, H., & Ramirez-Ruiz, E. 2014, *ApJ*, **783**, 23
 Guillochon, J., & Ramirez-Ruiz, E. 2013, *ApJ*, **767**, 25
 Guillochon, J., & Ramirez-Ruiz, E. 2015, *ApJ*, **809**, 166
 Guillochon, J., Ramirez-Ruiz, E., Rosswog, S., & Kasen, D. 2009, *ApJ*, **705**, 844
 Hayasaki, K., Stone, N., & Loeb, A. 2016, *MNRAS*, **461**, 3760
 Holoien, T. W.-S., Kochanek, C. S., Prieto, J. L., et al. 2016a, *MNRAS*, **463**, 3813
 Holoien, T. W.-S., Kochanek, C. S., Prieto, J. L., et al. 2016b, *MNRAS*, **455**, 2918
 Holoien, T. W.-S., Prieto, J. L., Bersier, D., et al. 2014, *MNRAS*, **445**, 3263
 Hung, T., Gezari, S., Blagorodnova, N., et al. 2017, *ApJ*, **842**, 29
 Jones, E., Oliphant, T., & Peterson, P. 2001, SciPy: Open Source Scientific Tools for Python, <http://www.scipy.org/>
 Kesden, M. 2012, *PhRvD*, **86**, 064026
 Kippenhahn, R., Weigert, A., & Weiss, A. 2012, *Stellar Structure and Evolution*, (2nd ed.; Berlin: Springer)
 Kochanek, C. S. 2016, *MNRAS*, **458**, 127
 Komossa, S. 2015, *JHEAp*, **7**, 148
 Laguna, P., Miller, W. A., Zurek, W. H., & Davies, M. B. 1993, *ApJL*, **410**, L83
 Law-Smith, J., MacLeod, M., Guillochon, J., Macias, P., & Ramirez-Ruiz, E. 2017a, *ApJ*, **841**, 132
 Law-Smith, J., Ramirez-Ruiz, E., Ellison, S. L., & Foley, R. J. 2017b, *ApJ*, **850**, 22
 Leloudas, G., Fraser, M., Stone, N. C., et al. 2016, *NatAs*, **1**, 0034
 Lodato, G., King, A. R., & Pringle, J. E. 2009, *MNRAS*, **392**, 332
 MacLeod, M., Guillochon, J., & Ramirez-Ruiz, E. 2012, *ApJ*, **757**, 134
 Magorrian, J., & Tremaine, S. 1999, *MNRAS*, **309**, 447
 Merloni, A., Dwelly, T., Salvato, M., et al. 2015, *MNRAS*, **452**, 69
 Mockler, B., Guillochon, J., & Ramirez-Ruiz, E. 2018, *ApJ*, submitted (arXiv:1801.08221)
 Paxton, B., Bildsten, L., Dotter, A., et al. 2011, *ApJS*, **192**, 3
 Phinney, E. S. 2018, in IAU Symp. 136, *The Center of the Galaxy*, ed. M. Morris (Dordrecht: Kluwer Academic), 543
 Ramirez-Ruiz, E., & Rosswog, S. 2009, *ApJL*, **697**, L77
 Rees, M. J. 1988, *Natur*, **333**, 523
 Roth, N., Kasen, D., Guillochon, J., & Ramirez-Ruiz, E. 2016, *ApJ*, **827**, 3
 Saxton, R. D., Read, A. M., Esquej, P., et al. 2012, *A&A*, **541**, A106
 Shiokawa, H., Krolik, J. H., Cheng, R. M., Piran, T., & Noble, S. C. 2015, *ApJ*, **804**, 85
 Strubbe, L. E., & Quataert, E. 2009, *MNRAS*, **400**, 2070
 van der Walt, S., Colbert, S. C., & Varoquaux, G. 2011, *CSE*, **13**, 22
 Wyrzykowski, Ł., Zieliński, M., Kostrzewa-Rutkowska, Z., et al. 2017, *MNRAS*, **465**, L114